

**ENHANCING SOLID PROPELLANTS WITH ADDITIVELY
MANUFACTURED REACTIVE COMPONENTS AND MODIFIED
ALUMINUM PARTICLES**

by

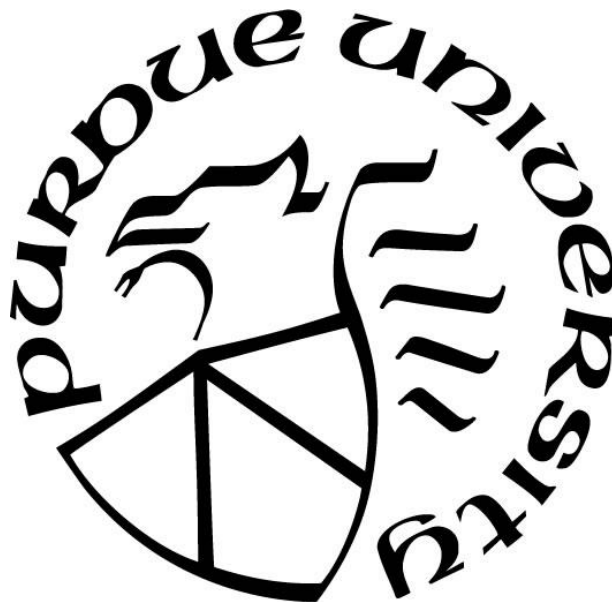
Diane Collard

A Dissertation

Submitted to the Faculty of Purdue University

In Partial Fulfillment of the Requirements for the degree of

Doctor of Philosophy



School of Mechanical Engineering

West Lafayette, Indiana

August 2021

THE PURDUE UNIVERSITY GRADUATE SCHOOL
STATEMENT OF COMMITTEE APPROVAL

Dr. Steven F. Son, Co-chair

School of Mechanical Engineering

Dr. Terrence R. Meyer, Co-chair

School of Mechanical Engineering

Dr. Jeffrey F. Rhoads

School of Mechanical Engineering

Dr. Timothée L. Pourpoint

School of Aeronautics and Astronautics

Approved by:

Dr. Nicole L. Key

*Dedicated to all of my family who have supported me through my endeavors, especially my mom
who built me up from Day 1.*

ACKNOWLEDGMENTS

This work would not be possible without the help and support of my advisors, Profs. Steve Son and Terrence Meyer. I would also like to thank Prof. Jeff Rhoads for his advice regarding this work and my time with the additive manufacturing of energetic materials group.

TABLE OF CONTENTS

LIST OF TABLES	7
LIST OF FIGURES	8
NOMENCLATURE	10
ABSTRACT.....	11
1. TAILORING THE REACTIVITY OF PRINTABLE Al/PVDF FILAMENT	13
1.1 Introduction.....	13
1.2 Methods and Materials.....	15
1.2.1 Pelletization	17
1.2.2 Filament Preparation.....	18
1.2.3 3-D Printed Reactive Wires	18
1.2.4 Safety, Quality, and Combustion Analysis.....	19
1.3 Results and Discussion	20
1.3.1 Characterization of MA Al-PTFE/PVDF and nAl/PVDF	21
1.3.2 Porosity Analysis	22
1.3.3 Combustion Performance of Filaments and Prints	25
1.3.4 Shock Sensitivity Test	30
1.4 Conclusions.....	30
1.5 Acknowledgments.....	31
1.6 References.....	31
2. DYNAMIC X-RAY IMAGING OF ADDITIVELY MANUFACTURED REACTIVE COMPONENTS IN SOLID PROPELLANT	34
2.1 Introduction.....	34
2.2 Methods.....	36
2.2.1 Reactive Wires	36
2.2.2 Propellant Formulation	38
2.2.3 X-ray Radiography	38
2.3 Results.....	40
2.4 Conclusions.....	47
2.5 Acknowledgments.....	47

2.6	References	47
3.	EXTRUSION OF AP COMPOSITE PROPELLANT WITH SELF-ALIGNED REACTIVE FIBERS	51
3.1	Introduction.....	51
3.2	Materials and Methods.....	53
3.3	Results and Discussion	56
3.4	Conclusions.....	63
3.5	Future Work	63
3.6	Acknowledgments.....	64
3.7	References.....	64
4.	FLASH AND LASER IGNITION OF Al/PVDF FILMS AND ADDITIVELY MANUFACTURED IGNITERS FOR SOLID PROPELLANT	68
4.1	Introduction.....	69
4.2	Experimental Methods	70
4.3	Results and Discussion	72
4.4	Conclusions.....	79
4.5	Acknowledgments.....	80
4.6	References.....	80
5.	SUMMARY.....	82
	APPENDIX A. SUPPLEMENTAL MATERIAL: TAILORING THE REACTIVITY OF PRINTABLE Al/PVDF FILAMENT	83
	APPENDIX B. SUPPLEMENTAL MATERIAL: DYNAMIC X-RAY IMAGING OF ADDITIVELY MANUFACTURED REACTIVE COMPONENTS IN SOLID PROPELLANT	85

LIST OF TABLES

Table 1.1. Products predicted using NASA CEA for a stoichiometric loading of MA Al-PTFE by mass.....	16
Table 1.2. Test matrix of Al/PVDF formulations.	17
Table 1.3. Porosity analysis of 32.2 wt.% MA Al-PTFE/PVDF and 20 wt.% nAl/PVDF.....	24
Table 1.4. The burning rates of filaments at ideal stoichiometric ratios.....	26
Table 1.5. The burning rates of printed lines of MA Al-PTFE/PVDF and 20 wt.% nAl/PVDF..	28
Table 1.6. The burning rates of filaments of varying nAl; μ Al fuel ratios.	30
Table 2.1. Linear regressions of volumetric consumption.....	46
Table 3.1. Average angle deviation from Z-axis aligned with the extrusion direction and substrate.	57
Table 4.1. Flash ignition delays and propagation modes.....	77
Table 4.2. Laser ignition delays and propagation modes.....	79

LIST OF FIGURES

Figure 1.1. DSC/TGA for (a) 20 wt.% nAl/PVDF and (b) MA Al-PTFE/PVDF.	21
Figure 1.2. MicroCT scans of MA Al-PTFE/PVDF (a) pellet, (b) filament, (c) 6-layer printed line, and nAl/PVDF (d) pellet, (e) filament, (f) 6-layer printed line.	23
Figure 1.3. Still frames and burning rate trace of MA Al-PTFE/PVDF burning in air at atmospheric conditions.	26
Figure 1.4. Still frames and burning rate trace of 20 wt.% nAl/PVDF burning in air at atmospheric conditions.	26
Figure 1.5. Still frames of burning printed lines of (a) MA Al-PTFE/PVDF and (b) 20 wt.% nAl/PVDF.	27
Figure 1.6. Average burning rates and associated standard deviations of filaments as a function of nAl content in comparison with other work [13].	28
Figure 1.7. (a) Average filament burning rates with associated standard deviations within individual batches of varying nAl mass fraction in fuel and (b) batch-averaged burning rates with associated standard deviations across multiple batches of filaments compared with previous work [12].	29
Figure 2.1. Narrow U-shape, pitchfork, and V-shape reactive wire geometries (units in mm).	37
Figure 2.2. Four printed 5 mm wide nAl/PVDF U-shapes embedded in cast propellant.	38
Figure 2.3. X-ray radiography configuration.	39
Figure 2.4. Cross-sections of microCT reconstructions of MA Al-PTFE/PVDF a) filament and b) printed V-shape strands cast in propellant.	41
Figure 2.5. Radiographic progressions of a) baseline (no wires), b) inert copper wire, c) MA Al-PTFE/PVDF filament, and d) nAl/PVDF filament in propellant strands with frames every 3 s.	42
Figure 2.6. Radiographic progression of narrow and wide pitchforks with frames every 1.2 s.	43
Figure 2.7. Radiographic progression of narrow and wide V-shapes with frames every 1.2 s.	43
Figure 2.8. Radiographic progression of narrow and wide U-shapes with frames every 1.2 s.	44
Figure 2.9. Volumetric consumption of (a) baseline and embedded filaments, (b) narrow pitchfork, (c) U-shapes, and (d) V-shapes with respective linear fits.	45
Figure 3.1. Reactive Al/PVDF fibers of 1, 3, 5, 7 AR.	53
Figure 3.2. Preview schematic of extrusion path.	54
Figure 3.3. Schematic of dual-view dynamic X-ray imaging system.	56
Figure 3.4. Underside of a cured extruded sample with 7 AR fibers.	57

Figure 3.5. Microscopic images of a slice of propellant with 7 AR fibers.	58
Figure 3.6. A failed 45° 5 AR propellant deflagration test with nail polish as an inhibitor.	58
Figure 3.7. A 45° 5 AR propellant deflagration test with sample encased in epoxy in a cuvette cell.	59
Figure 3.8. AP propellant burning rates with fibers of various aspect ratios oriented vertically within the strand.....	60
Figure 3.9. AP propellant burning rates with 5 AR fibers of various orientation within the strand.	61
Figure 3.10. Tomographic reconstruction of in-situ dual-view X-ray of reacting a) vertical, b) 45°, c) horizontal 5 AR propellant strand with frames 0.25 s apart.	62
Figure 4.1. The experimental setup associated with the experiments for (a) flash ignition and (b) laser ignition.....	71
Figure 4.2. Microscopic images of (a) the top of a printed nAl layer (b) a dual layer igniter with one layer of nAl on top of one layer of μ Al.....	73
Figure 4.3. The minimum ignition energy of films at varying concentrations of nAl and μ Al fuel.	73
Figure 4.4. Profilometer measurements obtained from nAl films and printed 1 nAl. The average total length is a numerical integration of the surface profile and is used to get an estimate of the total length exposed to the flash. Integrations were done over a 1 mm length portion of the data and averaged.....	74
Figure 4.5. The progression of a printed 1 nAl igniter exhibiting a rough transition between ignition of the nAl/PVDF and propellant.	75
Figure 4.6. The flash ignition delays of printed igniters with the percentage of smooth transitions indicated.	76
Figure 4.7. The progression of a printed 1 nAl x 1 μ Al igniter exhibiting a smooth transition between the first light on the igniter and the steady burning of the propellant.	77
Figure 4.8. Laser ignition delays of printed igniters with the percentage of samples with smooth transitions indicated.	78

NOMENCLATURE

a	=	empirically defined pre-exponential factor (cm/s atm ⁿ)
C	=	modifying constant
F	=	drag force (N)
L	=	length of a flat plate (cm)
MW	=	molecular weight (g/mol)
n	=	pressure exponent
P	=	pressure (atm)
r	=	burning rate (cm/s)
R	=	gas constant (cm ³ atm/K mol)
T	=	temperature (K)
u	=	gas velocity (cm/s)
W	=	width of a flat plate (cm)
ρ	=	density (g/cm ³)
μ	=	dynamic viscosity (P)

Subscripts

be	=	enhanced rate of reactive
b	=	bulk propellant
g	=	gas phase
c	=	condensed phase
mix	=	mixture in gas phase
u	=	universal

ABSTRACT

A variety of methods have been developed to enhance solid propellant burning rates, including adjusting oxidizer particle size, modifying metal additives, tailoring the propellant core geometry, and adding catalysts or wires. Fully consumable reactive wires embedded in propellant have been used to increase the burning rate by increasing the surface area; however, the manufacture of propellant grains and the observation of geometric effects with reactive components has been restricted by traditional manufacturing and viewing methods. In this work, a printable reactive filament was developed that is tailorable to a number of use cases spanning reactive fibers to photosensitive igniters. The filament employs aluminum fuel within a printable polyvinylidene fluoride matrix that can be tailored to a desired burning rate through stoichiometry or aluminum fuel configuration such as particle size and modified aluminum composites. The material is printable with fused filament fabrication, enabling access to more complex geometries such as spirals and branches that are inaccessible to traditionally cast reactive materials. However, additively manufacturing the reactive fluoropolymer and propellant together comes attendant with many challenges given the significantly different physical properties, particularly regarding adhesion. To circumvent the challenges posed by multiple printing techniques required for such dissimilar materials, the reactive fluoropolymer was included within a solid propellant carrier matrix as small fibers. The fibers were varied in aspect ratio (AR) and orientation, with aspect ratios greater than one exhibiting a self-alignment behavior in concordance with the prescribed extrusion direction. The effective burning rate of the propellant was improved nearly twofold with 10 wt.% reactive fibers with an AR of 7 and vertical orientation.

The reactive wires and fibers in propellant proved difficult to image in realistic sample designs, given that traditional visible imaging techniques restrict the location and dimensions of the reactive wire due to the necessity of an intrusive window next to the wire, a single-view dynamic X-ray imaging technique was employed to analyze the evolution of the internal burning profile of propellant cast with embedded additively manufacture reactive components. To image complex branching geometries and propellant with multiple reactive components stacked within the same line of sight, the dynamic X-ray imaging technique was expanded to two views. Topographic reconstructions of propellants with multiple reactive fibers showed the evolution of the burning surface enhanced by the geometric effects caused by the faster burning fibers. These dual-view

reconstructions provide a method for accurate quantitative analysis of volumetric burning rates that can improve the accessibility and viability of novel propellant grain designs.

1. TAILORING THE REACTIVITY OF PRINTABLE Al/PVDF FILAMENT

D. N. Collard, T. J. Fleck, J. F. Rhoads, S. F. Son, “Tailoring the reactivity of printable Al/PVDF filament,” *Combust. Flame*, vol. 223, pp. 110–117, 2021.

Within the energetic materials and additive manufacturing (AM) communities, a number of aluminum/fluoropolymer (Al/FP) combinations have been identified for their suitability in various additive manufacturing techniques. For practical applications, such as in the case of a reactive wire or core in solid propellant, a range of selectable reactivity within a given Al/FP selection is needed. The purpose of this study was to alter the reactivity of aluminum/polyvinylidene fluoride (Al/PVDF) to produce a range of consistent burning rates, enabling the design of a printable reactive filament suitable for use as a reactive propellant core, or in other related applications. Three potential methods of tailoring the burning rate of Al/PVDF filaments were investigated: 1) selecting different aluminum fuel particles, 2) adjusting the stoichiometry of the material, and 3) changing the fuel particle size ratio from pure micro- to pure nano-aluminum. Reactive filaments consisting of PVDF and either mechanically activated aluminum-polytetrafluoroethylene (MA Al-PTFE), nanoscale aluminum (nAl), or mixtures of nano- and micro-aluminum (nAl:μAl) were tested to assess reaction speeds as well as intra- and inter-batch variability. Differential scanning calorimetry, thermogravimetric analysis, drop weight impact testing, friction testing, and porosity analysis were conducted on select materials. Filaments of 20 wt.% nAl/PVDF and 32.2 wt.% MA Al-PTFE/PVDF were printed using a material extrusion method into strands with dimensions, porosities, and burning rates comparable to their filament feedstock. This study determined that the selection of fuel particles and stoichiometry could reliably produce moderate burning rates between 17 and 40 mm/s. The burning rates of the mixed formulations were inconsistent in the mid-range (20-30 mm/s) with significant deviation indicating a threshold phenomenon potentially related to a shift from a slower to faster reaction mode.

1.1 Introduction

Additive manufacturing (AM) offers several advantages over traditional manufacturing methods, from the production of complex geometries to the precise manufacture of tunable

microstructures [1]. Traditional propellant manufacturing techniques that require the removal of a casting core limit potential core perforation geometries. Recently, AM has been used in propellant applications to create complex bore shapes such as stars, helices, and branching perforations [2–5]. Furthermore, the ability to adjust the core perforation in-situ with consumable reactive “wires,” which also contribute energetically to the propellant burning, has been demonstrated [6]. However, the manufacturing method utilized in [6] of pressing the material into foils or reactive wires limited the wires to simple geometries. Using a printable reactive material would open a new facet of propellant optimization wherein complex solid reactive cores could be embedded or printed into propellant and used to open perforations in-situ. Reactive wires could be additively manufactured with Fused Filament Fabrication (FFF), a material extrusion technique wherein pellets of thermoplastics are made into filaments and printed layer-by-layer through a heated extruder head. This requires the development of a printable energetic material with sufficient reactivity to open a perforation, while not compromising the structural integrity of the propellant grain.

In the energetic materials and AM communities, aluminum/fluoropolymer (Al/FP) combinations have received appreciable attention due to the combination of fluorine’s strong oxidative properties and the suitability of a number of fluoropolymers for a variety of printing techniques [7–13]. The oxidation strength of fluorine-based species is comparable to, or greater than, that of chlorine [14]. Additionally fluorine-containing oxidizers in metalized energetic materials produce metal fluorides with high heats of formation and high vapor pressures that reduce two-phase flow losses [15]. The energy gained by the formation of metal fluorides over metal oxides makes fluorine an attractive component for energetic compositions. For example, AlF_3 brings 81% more energy per mole of aluminum than the formation of Al_2O_3 (ΔH_f° per mole of aluminum of $-1510 \text{ kJ mol}^{-1}$ vs. $-834.9 \text{ kJ mol}^{-1}$) [15]. An extensive amount of work has examined the reaction of Al with polytetrafluoroethylene (PTFE, C_2F_4) due to its high fluorine content (76% fluorine content by mass [16]). However, PTFE has limited practical application in AM due to PTFE’s insolubility in most solvents, high stiffness, and high melting temperature. To this end, the research focus has shifted to other fluoropolymers, including polyvinylidene fluoride (PVDF, $\text{C}_2\text{F}_2\text{H}_2$) and commercial copolymers. In recent years, Al/FPs have been selectively deposited in micro-Al (μAl) and nano-Al (nAl) formulations with direct write [7–10], electrospray deposition [11], and material extrusion methods [12–13].

A prior investigation by the authors demonstrated the functional capability of μAl /PVDF to be printed into multifunctional reactive structures [12]. However, a range of selectable reactivity is needed for practical applications, such as in the case of a reactive wire or core in solid propellant. For example, the formulation must achieve a faster burning rate than that of the surrounding propellant without compromising the structural integrity of the propellant. However, moderate burning rates may be desirable for the development of specific, highly tailored rocket thrust profiles or in the case of multiple reactive wires to potentially mitigate slivering. The purpose of this study was to alter the reactivity of printable Al/PVDF to consistently produce a range of burning rates, making available a means of designing printable reactive structures suitable for use in solid propellants to develop perforations in-situ.

1.2 Methods and Materials

Reactive wires were manufactured beginning with precursor powder and ending with 3D printed samples in three steps: 1) pelletization, 2) filament extrusion, and 3) printing with a FFF printer. To create an extrudable reactive material, aluminum fuels in the form of nAl (50 nm, Novacentrix Al-50-P), μAl (H3, 4.5 μm spherical particles, Valimet Inc.), and mechanically activated aluminum-polytetrafluoroethylene (MA Al-PTFE, Ref. [17]) were combined with polyvinylidene fluoride (PVDF, Kynar 711) in an acetone-dimethylformamide solution and dried to form pellets from the initial powders. The printer feedstock was created by extruding the pellets of thermoplastic material into a filament with a diameter under 1.75 mm, to ensure compatibility with most commercial printers. Through FFF, the filament was continuously passed through a heated extruder head to build a reactive wire layer by layer.

This study investigates the effects of particle size, stoichiometry, and the selection of Al fuel particles on the burning rate of Al/PVDF filaments and printed lines. To investigate the particle size effects of neat Al particles, nAl and μAl were mixed at nAl mass fractions of fuel of 0.25, 0.5, 0.625, and 0.75 and added to PVDF. The total aluminum fuel in the mixtures was kept at a solids loading of 20 wt.% active aluminum. This solids loading was previously determined to be close to the stoichiometric ratio [12]. For studying the effects of stoichiometry, pure nAl was mixed with PVDF at 10, 15, 17.5, and 20 wt.% active aluminum or equivalence ratios of 0.44, 0.71, 0.85, and 1.0, respectively. In addition to the previous formulations, samples of reactive filament were made with a modified aluminum fuel prepared by milling aluminum and PTFE

powders as detailed by Sippel et al. [17]. The samples tested used flakes of 40 min high energy mechanical activation 70:30 wt.% Al-PTFE. In an ideal reaction, all of the aluminum would be fully fluorinated and converted to AlF_3 , leading to the proposed simplified chemical balance $\text{Al} + 0.12\text{C}_2\text{F}_4 + 1.27\text{C}_2\text{F}_2\text{H}_2 \rightarrow \text{AlF}_3 + 2.77\text{C} + 1.27\text{H}_2$ and resulting in an estimated stoichiometric solids loading of 32.2 wt.% MA Al-PTFE. To better estimate the products of reaction of MA Al-PTFE with PVDF, the thermochemical code NASA CEA [18] was run with the material at the estimated ideal stoichiometry. Equilibrium products were determined for adiabatic combustion at atmospheric pressure. Only the predicted products calculated by CEA containing more than 1% mole fraction are reported in Table 1.1. Note that the ideal reaction ignores the partial fluorination of both hydrogen and aluminum. The production of AlF leads to a decrease in performance relative to the complete fluorination of aluminum to AlF_3 due to a decrease in released energy. Furthermore, hydrofluoric acid (HF) production at a large scale is both environmentally hazardous and corrosive rendering it further non-ideal. Adjusting the amount of MA Al-PTFE to minimize one of these products leads to the higher production of the other, so the ideal solids loading of 32.2 wt.% MA Al-PTFE was chosen for further use herein. In total, the nine formulations tested are summarized in Table 1.2. The following sections detail how the formulations were prepared and 3D printed.

Table 1.1. Products predicted using NASA CEA for a stoichiometric loading of MA Al-PTFE by mass.

Product of Reaction	Mole Fraction Predicted by CEA	Mole Fraction Predicted by Ideal Combustion
Carbon, C	0.4845	0.5496
Hydrogen fluoride, HF	0.2052	0.0000
Hydrogen gas, H_2	0.1095	0.2520
Aluminum monofluoride, AlF	0.0988	0.0000
Aluminum fluoride, AlF_3	0.0719	0.1984
Hydrogen, H	0.0191	0.0000

Table 1.2. Test matrix of Al/PVDF formulations.

Pure nAl Solids Loading	Mixtures of nAl and μ Al (x_{nAl} in Fuel)	Pure MA Al-PTFE Solids Loading
20 wt.%	0.25	32.2 wt.%
17.5 wt.%	0.5	
15 wt.%	0.625	
10 wt.%	0.75	

1.2.1 Pelletization

Pellets were made by dissolving agglomerated PVDF in a two solvent mixture of acetone (Fisher Chemical, Certified ACS) and dimethylformamide (DMF) (Anhydrous 99.8%, Sigma Aldrich) as detailed by Fleck et al. [12]. Each vial was designed to contain 2 g of Al/PVDF. To create a polymer precursor, solutions were agitated at an amplitude of 15% for 1 min using a digital sonifier (Branson Ultrasonics SF250). Then, the MA Al-PTFE, nAl, or nAl/ μ Al fuel was poured into the PVDF solution. For mixtures with nAl and μ Al, the nAl was added to the solutions first and sonicated for 1 min before adding the μ Al to break up agglomerates. Once the remainder of the Al fuel was added, all of the mixtures were sonicated for a second time to ensure uniform dispersion. Due to safety concerns, all of the Al/PVDF solutions were sonicated with a 1 min ON, 1 min OFF cycle for 10 min at an amplitude of 15% to disperse the fuel particles.

During sonication, some of the solvent evaporated and the mixture became thicker as it slowly began to gel. Two vials of material were then poured into a single metal weigh tin (Cole-Parmer UX-01018-28) for further drying to create slabs of material from which pellets were made. The MA Al-PTFE settled during evaporation, due to its large particle size and flake-like nature. To mitigate this dissolution, the weigh tins were placed on a shaker table (IKA KS 260 Basic) at 150 rpm until the solution began to gel (~45 min). The weigh tins were removed from the shaker table, stirred by hand, and dried for another 45 min before scoring with a razor blade into pellets approximately 2 mm x 2 mm x 2 mm in scale. The pellets were further dried for another 48 hr to ensure full solvent evaporation. For the other mixtures of nAl and μ Al, no further agitation was needed after sonication and the resulting material was scored into pellets approximately 2 h into the drying process.

1.2.2 Filament Preparation

A temperature-controlled single barrel screw extruder (Filabot, Original Filament Extruder) was used to manufacture 3D printable filaments from the Al/PVDF pellets. To address the potential safety hazards associated with the extrusion of energetic materials, the extruder setup was modified to enable remote operation as in prior work [12, 19]. Energetic pellets were loaded into one side of a divided funnel with inert purge pellets (Filabot Extruder Purge Compound) loaded on the other. A remotely operated slide was triggered to open the energetic material side of the funnel to the extruder hopper. To ensure the appropriate amount of mixing was achieved during the pellets' residence time in the extruder, energetic pellets were allowed to extrude for 25-30 min at a constant temperature of 195°C and screw rate of 35 rpm before introducing the purge compound to push the Al/PVDF material through the extruder. As the material exiting the extruder became more inert, the color became significantly lighter, indicating the extruder could be safely turned off and cleaned.

Since the extruder was remotely operated, a tension controller could not be attached, which caused a consistently oversized diameter. A 1.60 mm nozzle was used to keep the filament diameter below 1.75 mm (a common maximum diameter for most commercial FFF printers). Without a tension controller, the filament tended to have an elliptical cross-section. To mitigate this, the extruder was tilted and a Teflon slide attached. A cooling fan directed at the nozzle was used to prevent over-tensioning of the material as it cooled and re-solidified. Only samples of consistent diameter were used in experimentation. The melt viscosity increased as the aluminum particle size decreased, yielding smaller sections of testable material (~60% of the filament was usable for nAl/ PVDF versus ~80% for the μ Al/ PVDF material [12]).

1.2.3 3-D Printed Reactive Wires

Samples of MA Al-PTFE/PVDF and nAl/PVDF were printed with a Makerbot Replicator 2X into lines with approximate dimensions of 51 mm x 1.6 mm x 1.6 mm to facilitate comparison to raw filament and prior work with μ Al/PVDF [12]. The printing parameters were adjusted for each type of filament to produce dense samples. The print speed, extruder temperature, and primary layer height were found to be imperative to achieve consistent prints. Print speeds of 10 mm/s and a 75% first layer height (0.1125 mm) provided the best initial layer adhesion and surface

finish for all of the materials. Extruder temperatures of 220°C for MA Al-PTFE and 240°C for the nAl formulations resulted in prints with no significant surface defects. With smaller fuel particles loaded into the PVDF, the melt flow viscosity increased. This necessitated the increase of the printing temperature relative to formulations with larger particles, such as MA Al-PTFE. Similarly, MA Al-PTFE had a larger particle size than the μ Al and consistent printing was achieved at 10°C lower than that associated with μ Al in previous work [12]. Compared to standard ABS, PVDF has a low melt flow index, which necessitates a slower print speed. Likewise, due to the larger size and irregular shape of the MA Al-PTFE particles, the first layer height is crucial for the largest particles to stick to the build plate when deposited. To enhance the adhesion to the build surface, a combination of a BuildTak 3D Printing Surface and Elmer's All-Purpose Glue Stick was used on the build plate. For all of the materials, the build plate temperature was set to 120°C.

Similar to the extrusion processes, all of the printing was completed remotely in an adjacent control room and monitored with a live camera feed to minimize direct interaction with the filament. After the samples finished printing, the print head was purged with ABS filament until the extruded filament changed color indicating a transition to inert material.

1.2.4 Safety, Quality, and Combustion Analysis

To determine the onset of reaction temperature, differential scanning calorimetry and thermogravimetric analysis (DSC/TGA) were conducted on both 20 wt.% nAl/PVDF and MA Al-PTFE/PVDF using a TA Instruments SDT-Q600 Simultaneous DSC/TGA. Since PVDF has a low glass transition temperature ($\sim -42^\circ\text{C}$), a cycle for thermal preconditioning was not conducted [20]. Samples of ~ 2 mg were placed under argon gas flowing at 100 mL/min and tested from room temperature to 800°C with a temperature ramp of 10°C/min. Since these materials react on thermal analysis over the range of temperature tested, a subsequent cycle was used only to obtain an instrument baseline since the sample had been consumed in the prior cycle.

Friction and drop weight impact testing were conducted on 20 wt.% nAl/PVDF pellets. A modified Bruceton statistical analysis was used to reduce the friction data and identify a 50% go/no-go frictional force [21]. Since pellets rather than powders were tested, the experiment was conducted with a double stroke method: the first stroke smeared the pellet into the grooves of the strike plate and the second tested for initiation. No pellets ignited on the first stroke. Each double

stroke was recorded as a single test. Drop weight impact testing was conducted with the Neyer statistical method suggesting a subsequent drop height to find a probability of reaction of 50% (L_{50}). In total, 16 heights were tested with a setup tolerance of 0.64 cm.

Porosity plays a fundamental role in both the burn characteristics of the material and the consistency of subsequent printing and processing. Helium pycnometry (AccuPyc II 1340 Gas Displacement Pycnometer) and envelope pycnometry (GeoPyc 1360 Density Analyzer) were conducted to quantitatively estimate the open and closed porosity of the pellets, filaments, and prints. X-ray micro-computed tomography (Skyscan 1272 X-Ray MicroCT) was used to qualitatively determine pore shape and examine the porosity of the resulting pellets, filaments, and printed samples.

Combustion analysis was conducted on all of the filament formulations and the two printed line formulations. Strands 50 mm in length were held vertically on the stand by an alligator clip and ignited with a resistively heated 30 AWG NiChrome wire wrapped three times around the top of the strand. The burning rates were determined by recording the reaction with a high-speed camera (Phantom v10) at 1000 fps and exposure of 990 μ s followed by post-processing with Matlab. The Matlab script recorded instantaneous burning rates by tracking the burning surface over a user-defined interval, then proceeded to fit a linear regression to derive the average burning rate for the strand. A minimum of 5 samples were recorded for each batch of material to gauge repeatability.

1.3 Results and Discussion

For the reliable selection of printable reactive wires for the in-situ development of center perforations in propellant, the burning rate of the material must be consistent and repeatable. This necessitates high inter- and intra-batch repeatability and printed parts with a good infill which is devoid of defects, such as concentrated or interconnected porosity. The results in the following sections highlight three methods for tailoring the reactivity of Al/PVDF filaments by material selection, stoichiometry, and fuel particle size ratios and present a quality analysis of the material at each stage of the process.

1.3.1 Characterization of MA Al-PTFE/PVDF and nAl/PVDF

The thermal characteristics of the energetic material were determined before processing pellets into printable filaments. The location of the first exotherm and the onset temperature is crucial for defining a safe operating temperature range for extrusion. As shown in the DSC/TGA trace in Figure 1.1, the onset of the first exotherm, identified as the pre-ignition reaction (PIR) [22–23], for both the MA Al-PTFE/PVDF and nAl/PVDF material was approximately 375°C, while the melting temperature of neat PVDF is around 165°C [24]. In the first decomposition step, PVDF fluorinates the oxide shell and promotes reaction with the aluminum core at higher temperature. In the second decomposition, the remaining PVDF intermediates react with aluminum. The decomposition peaks in Figure 1.1a remain relatively discrete compared to Figure 1.1b, due to the failure to fully propagate the reaction. The maximum operating temperature was set to 240°C during printing to maintain a consistent flow while remaining below the reaction onset temperature.

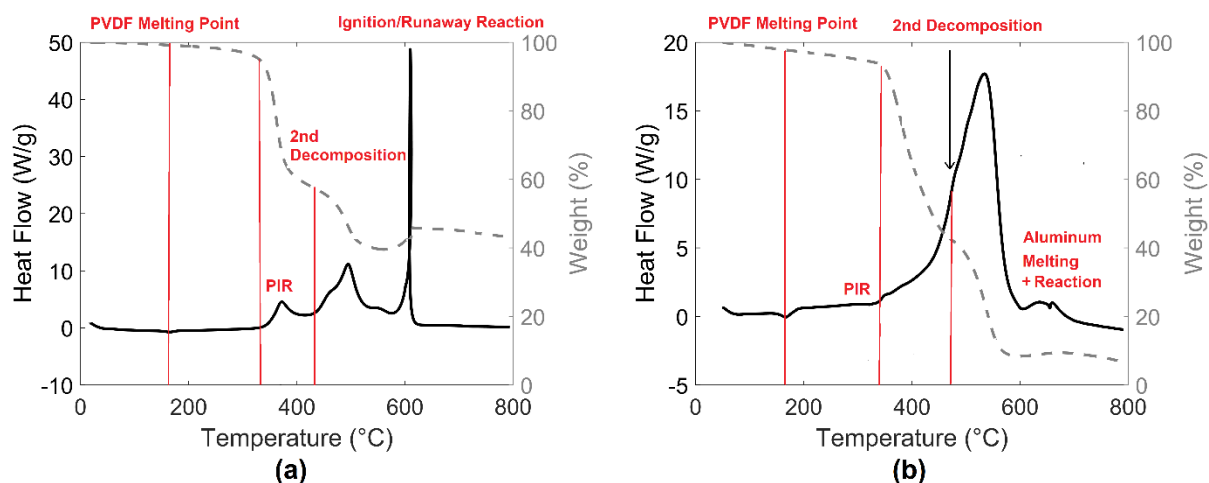


Figure 1.1. DSC/TGA for (a) 20 wt.% nAl/PVDF and (b) MA Al-PTFE/PVDF.

The sensitivity of energetic materials with nanoscale inclusions has been shown to be higher than their microscale counterparts, therefore 20 wt.% nAl/PVDF was subjected to friction and drop weight impact testing. The friction testing resulted in an F_{50} of 228.6 N with a standard deviation of 19.6 N, which is less sensitive than hexagen (RDX), octagon (HMX), and pentaerythritol tetranitrate (PETN), but more sensitive than ammonium perchlorate (AP), ammonium nitrate (AN) and other oxidizers [25]. The drop weight impact testing yielded an L_{50}

of 53.9 cm with a standard deviation of 10.4 cm, which is comparable to RDX [26]. With these sensitivity results, extrusion was deemed feasible with the additional safety precaution of remote operation.

1.3.2 Porosity Analysis

A major concern of additive manufacturing applied to reactive materials is the consistency of the prints. The infill of an additively manufactured part must be differentiated from printed bead porosity, the former directly related to the printer operation while the latter receives contributions from the inherent characteristics of the material. Suboptimal print settings may lead to print defects, such as interlayer debonding and gaps; which, in turn, result in inconsistent combustion performance. The presence of voids in a sample typically leads to an increased effective burning rate. As the reaction front encounters a void, it will proceed into the pore, convectively transport heat forward, and increase the surface area available to the reaction, thereby increasing the effective burning rate. In the case of poor infill resulting in a gap, a reaction front can enter and rapidly propagate through the length of the void, which can lead to over-pressurization and further crack propagation to disastrous effect. Thus, an ideal quality print consists of high infill, a thin flame front, and consistent flame propagation.

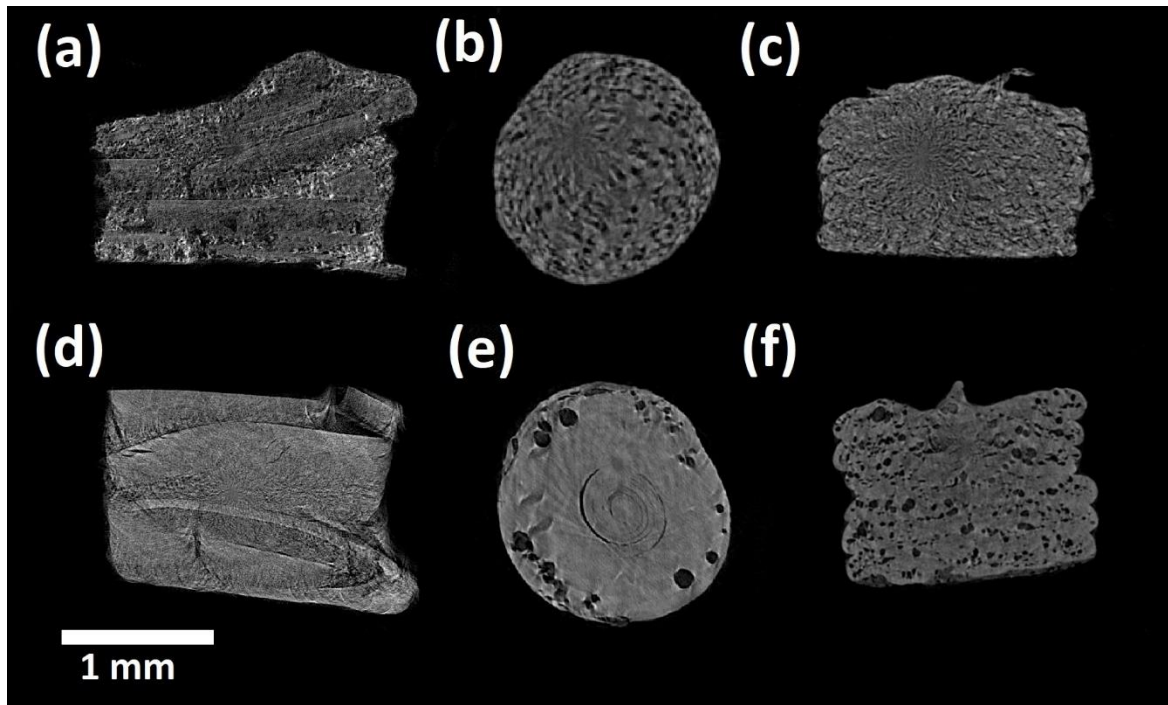


Figure 1.2. MicroCT scans of MA Al-PTFE/PVDF (a) pellet, (b) filament, (c) 6-layer printed line, and nAl/PVDF (d) pellet, (e) filament, (f) 6-layer printed line.

As shown by the X-ray microCT scans in Figure 1.2, where lighter pixels indicate denser material and the scale is consistent throughout all parts of the composite image, the energetic materials have a degree of porosity inherent to each stage of the process. The printed lines in Figure 1.2(c) and (f) show proper interfacial adherence and good infill, with a bead porosity of approximately 10% for both MA Al-PTFE and nAl prints. Figure 1.2(b) and (e), MA Al-PTFE filaments are more porous throughout than nAl, which may be attributed to the larger size and irregular shape of the particles, as irregular particles do not pack as neatly relative to spherical particles, except in more favorable size distributions. The filament of nAl exhibits a concentration of pores towards the surface, which may be an artifact of the slow extrusion speeds and the high viscosity of the material. Ideally, the material would be fully dense with little to no porosity. Although the filaments and prints are non-ideal, the pores remain segregated and do not link together to form channels through which the flame can convectively propagate. This was validated by the burning rate measurements which are shown to be linear in the following section in Figures 1.3 and 1.4.

Table 1.3. Porosity analysis of 32.2 wt.% MA Al-PTFE/PVDF and 20 wt.% nAl/PVDF.

Sample	Helium Pycnometer Closed Porosity (%)	Envelope Pycnometer Total Porosity (%)	microCT Analysis Total Porosity (%)
MA Al-PTFE/PVDF			
Pellet	0.75±1.05	56.34±0.02	55.93
Filament	20.25±1.67	23.69±0.69	19.05
Print	9.68±0.12	22.97±0.83	10.87
nAl/PVDF			
Pellet	1.51±0.01	45.58±0.20	45.30
Filament	10.28±0.01	14.30±0.18	11.49
Print	10.80±0.02	16.87±0.18	15.80
PVDF			
Pellet	0.39±0.01	39.21±0.20	
Filament	0.81±0.01	1.82±0.06	
Print	0.62±0.01	0.38±0.20	

Quantitative porosity analysis was conducted on the microCT reconstructions and compared to the gas pycnometer and envelope density analyzer results (see Table 1.3). The same six filament samples from the same batch of filament and six individually printed lines were tested using both a gas pycnometer and an envelope density analyzer. Gas pycnometry was used to determine the closed porosity of the samples as helium can enter into pores open to the surface, eliminating most open porosity. Total porosity—the sum of open and closed porosity—was examined with both computationally analyzed microCT images and an envelope density analyzer that employed Dry Flo[®], a highly flowable sand-like material of small rigid spheres with a d_{50} of approximately 150 μm .

The pellets were shown to have the highest open porosity, likely due to a number of connected pores that channel solvent when evaporating. Closed porosity increased and open porosity decreased when the pellets were processed into filaments. As filaments were printed, the closed porosity of the MA Al-PTFE/PVDF samples decreased significantly, likely due to the material rearrangement through the small nozzle of the print head. Even though more open porosity is introduced due to the rough sides of the print, the reduction in closed porosity through rearrangement is greater, leading to a decrease in total porosity between the MA Al-PTFE filaments and prints. The filaments and prints of the nAl/PVDF samples showed no significant change in closed porosity, suggesting less rearrangement when passed through the nozzle of the

printer. Open porosity increased between the nAl/PVDF filament and print, which may be attributed to the inherently rough sides of the prints.

Due to Dry Flo[®] being a solid medium of rigid diameter spheres, the envelope density may be over-predicted due to packing factors. However, when testing samples close to maximum density, the envelope density analyzer may be subject to systematic errors, culminating in a non-physical result, as seen in the neat PVDF prints where the closed porosity was found to be greater than the total porosity. The low porosity of the PVDF printed lines was verified using water displacement (ASTM D792-13), resulting in a porosity measurement of $0.73 \pm 0.80\%$. All of the porosity values of the printed PVDF were consistently found to be less than 1%. Porosity analysis of microCT scans depends highly on the user-defined mesh resolution. Higher resolutions may cut into open pores, resulting in an underprediction of open porosity and vice versa. These factors may explain the discrepancies that arose in the porosity analysis of the MA Al-PTFE/PVDF prints and the nAl/PVDF pellets. As such, the quantities in Table 1.3 should be used as a means of comparison within the materials tested rather than taken as absolutes.

1.3.3 Combustion Performance of Filaments and Prints

Three potential methods of tailoring the burning rate of Al/PVDF filaments were tested: 1) selecting different aluminum fuel particles, 2) adjusting the stoichiometry, and 3) changing the fuel particle size ratio. First filaments containing nAl and MA Al-PTFE were compared to previously investigated μ Al filaments near ideal stoichiometric ratios. The flake-like MA Al-PTFE particles are nanocomposites of aluminum with small inclusions of PTFE and show faster burning rates than μ Al. During reaction, the PTFE gasifies first, breaking the large flakes apart into several smaller constituents and increasing the rate of combustion relative to the μ Al formulation [17]. Similarly, the nAl filaments react faster than μ Al due to the smaller size of the fuel particles, which lowers the distance the oxidizer must diffuse to come into contact with the aluminum. As shown in Table 1.4, the highest burning rates were achieved with nAl, followed by the MA Al-PTFE filaments. For each formulation, two batches of material with a sample of six individual filaments were tested. Both nAl and MA Al-PTFE filaments outperformed the previously tested μ Al [12]. If these filaments were to be tested at higher pressures, the burning rates would be expected to increase relative to a characteristic pressure exponent. Furthermore, differences of the exponent may elucidate the dominant combustion mode of each formulation.

Table 1.4. The burning rates of filaments at ideal stoichiometric ratios.

Fuel	Sample Size per Batch	Average Diameter (mm)	Average Burning Rate (mm/s)	St. Dev. (mm/s)
nAl	6	1.51	40.6	2.5
MA Al-PTFE	6	1.49	24.3	1.4
μ Al ¹	6	1.53	18.7	1.3

¹Reported in Fleck et al., 2017 [12]

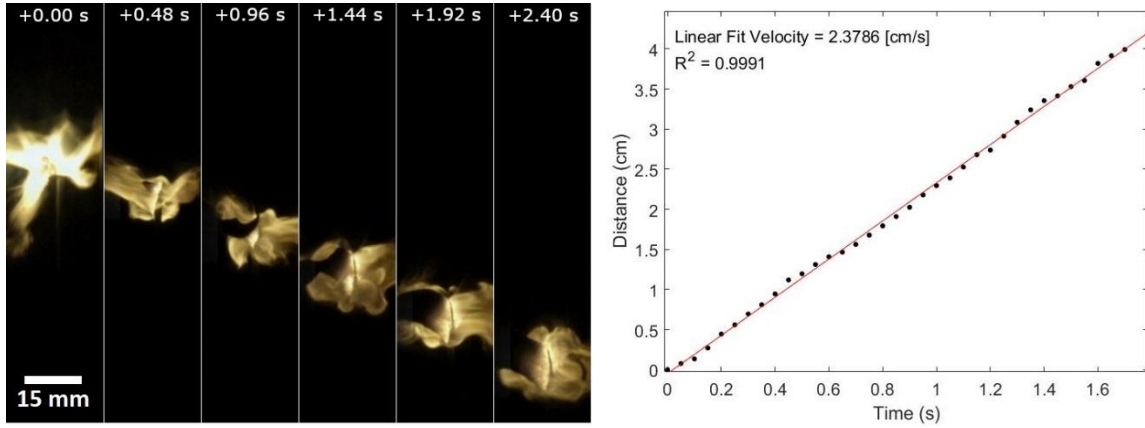


Figure 1.3. Still frames and burning rate trace of MA Al-PTFE/PVDF burning in air at atmospheric conditions.

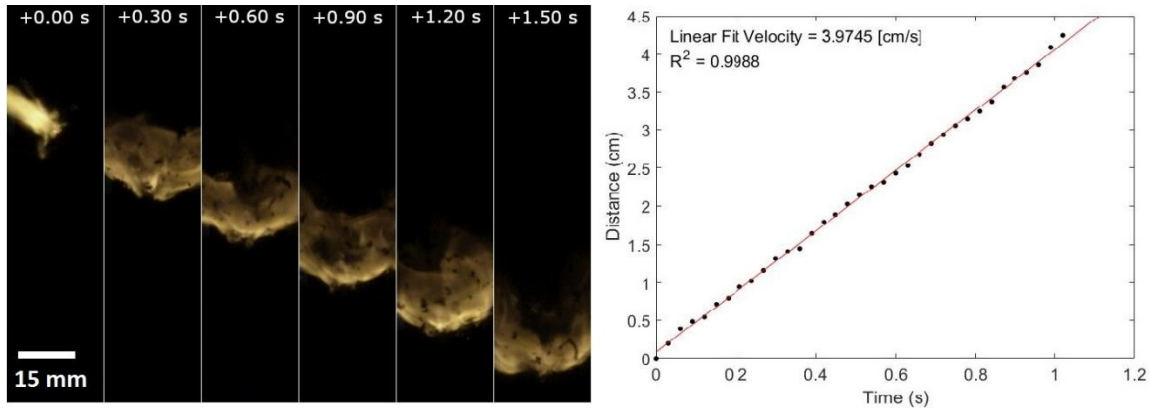


Figure 1.4. Still frames and burning rate trace of 20 wt.% nAl/PVDF burning in air at atmospheric conditions.

The linear burning rates shown in Figures 1.3 and 1.4 indicate that the filament material had a uniform distribution. If uniform mixing was not achieved in fabrication, the burning rate would be inconsistent as the reaction front encountered regions of fuel rich or fuel lean conditions. Furthermore, if the porosity throughout the filament sample fluctuated significantly, irregular or uneven burning rates would be produced, yielding a lower fit around the average burning rate

shown by the linear fit on the right of Figures 1.3 and 1.4. Further supplemental tests examining burning rates and porosity are provided in the supplementary material. A distinct difference in soot generation was observed between filaments. As shown in Figure 1.3, the MA Al-PTFE filaments produced continuously snaking soot strands. Continuous soot strands were only generated in filaments of MA Al-PTFE and mixtures of nAl/ μ Al with 50% or greater μ Al by mass. As seen in Figure 1.4, filaments with fuel mixtures with less than 50% μ Al and all nAl-only formulations produced fine soot. The fine soot was blown apart near the surface of the burn and pushed away rapidly. As 15 wt.% nAl propagates at approximately the same speed as μ Al and 0.25 nAl, yet the former exhibits fine soot and the latter two form continuous soot, the mode of soot generation is correlated to the size of the aluminum particles rather than propagation speed. The finer particles of nAl may lead to rapid local reactions that disruptively blow apart the soot and prevent continuous strands from forming.

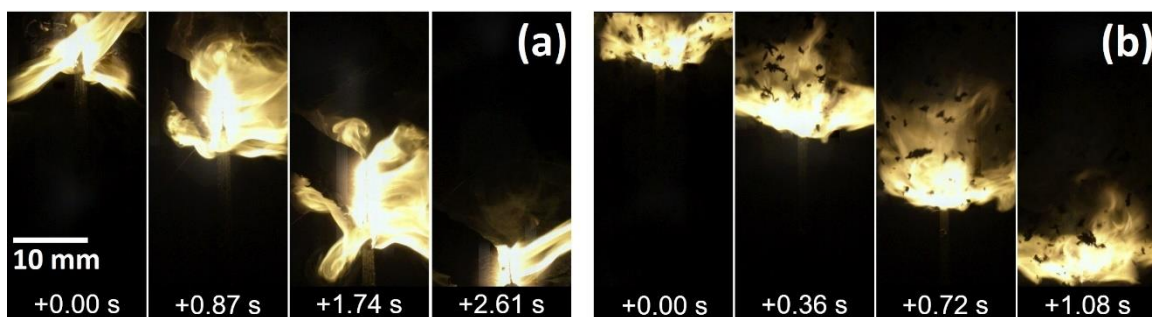


Figure 1.5. Still frames of burning printed lines of (a) MA Al-PTFE/PVDF and (b) 20 wt.% nAl/PVDF.

Printed lines of MA Al-PTFE/PVDF and 20 wt.% nAl/PVDF were combusted in the same setup as the filaments. Qualitatively, the flame fronts and manner of soot generation of the printed lines in Figure 1.5 are comparable to the filaments in Figures 1.3 and 1.4. The average burning rates in Table 1.5 show no significant change from the filaments, further confirming good quality printed lines. The results were consistent with prior work in which μ Al/PVDF filaments and prints exhibited negligible differences in burning rates [12].

Table 1.5. The burning rates of printed lines of MA Al-PTFE/PVDF and 20 wt.% nAl/PVDF.

Fuel	Sample Size per Batch	Average Diameter (mm)	Average Burning Rate (mm/s)	St. Dev. (mm/s)
nAl	5	1.52	43.4	2.7
MA Al-PTFE	6	1.51	22.5	3.6

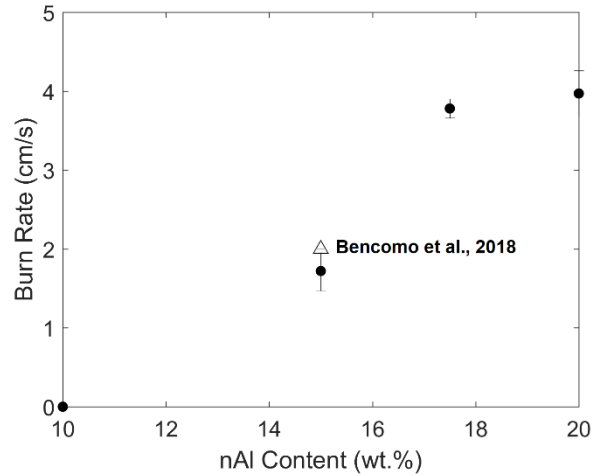


Figure 1.6. Average burning rates and associated standard deviations of filaments as a function of nAl content in comparison with other work [13].

The second method of altering the propagation speed was to vary the fuel to oxidizer ratio. Strips of pellet material at different nAl solids loadings were flame tested for self-propagation before extruding into filament. Starting at the ideal stoichiometric ratio corresponding to 20 wt.% nAl, the solids loading was reduced until the cast strips of material would no longer sustain burning. The material was found to no longer support self-propagating reaction at 10 wt.% nAl and only smoldered when held under a butane torch. The drop cast material was then extruded into filaments. Burning rates were collected for six filament samples of each formulation with an average diameter of 1.56 mm. In Figure 1.6, the burning rate rises to an apparent maximum as the solids loading of nAl approaches the estimated ideal stoichiometric ratio. The tested material also displays close agreement at 15 wt.% nAl as shown by Bencomo et al. [13].

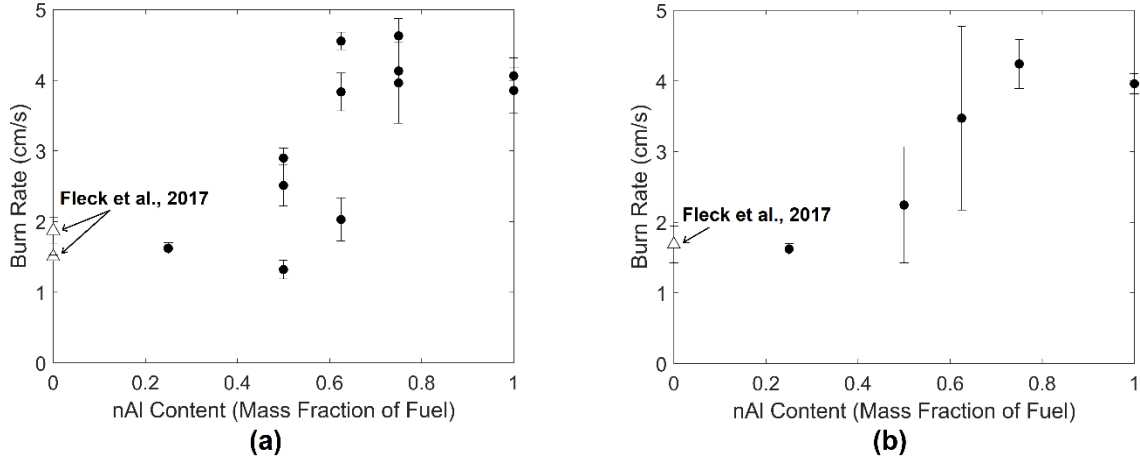


Figure 1.7. (a) Average filament burning rates with associated standard deviations within individual batches of varying nAl mass fraction in fuel and (b) batch-averaged burning rates with associated standard deviations across multiple batches of filaments compared with previous work [12].

The final method of altering the burning rate examined formulations with mixtures of nAl and μ Al fuel. These mixtures were added to PVDF at a solids loading of 20 wt.% at ratios ranging from pure μ Al to pure nAl. As shown in Table 1.6, multiple batches with similar sample sizes and diameters were tested to investigate the batch-to-batch variation. In Figure 1.7, the variability was determined not to be caused by batch-to-batch variation alone, as the inter-batch burning rate deviation increases drastically at 0.5 and 0.625 nAl before converging again at higher concentrations of nAl in the fuel. The trend of large deviations in the mid-range burning rates suggests a potential threshold phenomenon wherein the combustion mode changes from a slower (formulations with primarily μ Al) to faster mode (filaments with higher nAl content).

Table 1.6. The burning rates of filaments of varying nAl:μAl fuel ratios.

Composition (x_{nAl} in Fuel)	Batches	Sample Size per Batch	Average Diameter (mm)	Average Burning Rate ² (mm/s)	St. Dev. (mm/s)
1	2	6	1.51	39.7	2.9
0.75	3	7	1.56	42.4	3.5
0.625	3	7	1.60	34.7	13.0
0.50	3	7	1.56	22.2	7.5
0.25	1	7	1.55	16.2	0.8
0 ¹	2	6	1.53	16.8	2.6

¹Reported in Fleck et al., 2017 [12]

²Across all of the batches

Due to the potential thresholding behavior, a mixture of nAl and μAl cannot be reliably selected to produce a moderate burning rate between 17 and 40 mm/s. However, a moderate burning rate can be achieved by adjusting the stoichiometry of the filaments to a fuel-lean formulation or by using MA Al-PTFE. Thus, printable Al/PVDF filaments can be chemically tailored to achieve a range of reaction rates.

1.3.4 Shock Sensitivity Test

A printed 1 cm diameter by 1 cm high pellet of 20 wt.% nAl/PVDF was tested for shock sensitivity using a simple plate dent test. An RP-502 detonator with a PBX 9501 booster at 1.81g/cc of the same dimensions as sample and an aluminum witness plate were used for the tests. Two samples were tested in identical setups and neither showed evidence of detonation at this diameter or shock input.

1.4 Conclusions

Three methods for modifying the reaction rate of Al/PVDF were investigated to create a range of burning rates, allowing for tailored functionality. The highest burning rates of the formulations tested were achieved with 20 wt.% nAl and fuel mixtures with 0.75 nAl in PVDF. 0.25 nAl and pure μAl consistently had the lowest burning rates. Fuel lean mixtures of nAl/PVDF were suitable for selecting comparatively moderate burning rates between these lower and higher bounds. Mixtures of nAl/μAl could not reliably be used for moderate burning rates due to a

sensitive thresholding behavior, which may be related to a switch from slower to faster reaction modes.

A primary concern of additive manufacturing is print quality that results in full infill and retains the combustion properties of the feedstock material. In previous work, reactive $\mu\text{Al}/\text{PVDF}$ has been demonstrated as a printable energetic filament with combustion properties preserved between the filament feedstock and finished printed lines [12]. This work demonstrates the printability of 20 wt.% nAl/PVDF and 32.2 wt.% $\text{MA Al-PTFE}/\text{PVDF}$. With the proper print settings, these formulations yielded prints with good infill density and burning rates indistinguishable from their filament feedstock.

The small-scale tests investigated in this work lay the foundation for selectable reaction rates of Al/PVDF . However, for practical application, much work remains to be done to address the challenges of scaling to sample sizes on the order of centimeters and greater. Maintaining reasonable porosity and minimizing defects on these scales will be challenging and will require further refinement of the filament fabrication process.

1.5 Acknowledgments

The authors would like to thank the Center for Particulate Products and Processes at Purdue University for access to the X-ray microCT scanner. This work was supported by the National Science Foundation Graduate Research Fellowship Program grant number DGE-1333468 and AFOSR MURI award number FA9550-19-1-0008.

1.6 References

- [1] N.V. Muravyev, K.A. Monogarov, U. Schaller, I.V. Fomenkov, A.N. Pivkina, Progress in additive manufacturing of energetic materials: Creating the reactive microstructures with high potential of applications, *Propellants Explos. Pyrotech.*, 44 (2019) 941-969.
- [2] J. Fuller, D. Ehrlich, P. Lu, R. Jansen, J. Hoffman, Advantages of rapid prototyping for hybrid rocket motor fuel grain fabrication, 47th AIAA/ASME/SAE/ASEE Jt. Propuls. Conf. & Exhib., (2011) 1–10.
- [3] A. Bath, Performance Characterization of Complex Fuel Port Geometries for Hybrid Rocket Fuel Grains, *All Graduate Theses and Dissertations*. 1381 (2012). <https://digitalcommons.usu.edu/etd/1381>

- [4] C. Bauer, Y. Metsker, C. von Sethe, M. Mutschler, M. Bambauer, P. Lungu, M. Brandl, Application of additive manufacturing in solid and hybrid grain design, 52nd AIAA/SAE/ASEE Jt. Propuls. Conf., (2016) 1–13.
- [5] S.A. Whitmore, Three-dimensional printing of ‘green’ fuels for low-cost small spacecraft propulsion systems, *J. Spacecr. Rockets*, 55 (2018) 13–26.
- [6] S. Isert, C.D. Lane, I.E. Gunduz, S.F. Son, Tailoring burning rates using reactive wires in composite solid rocket propellants, *Proc. Combust. Inst.*, 36 (2017) 2283–2290.
- [7] F. Ruz-Nuglo, L. Groven, J.A. Puszynski, Additive manufacturing for energetic components and materials, 50th AIAA/ASME/SAE/ASEE Jt. Propuls. Conf., (2014) 1–7.
- [8] X. Li, P. Guerieri, W. Zhou, C. Huang, M.R. Zachariah, Direct deposit laminate nanocomposites with enhanced propellant properties, *ACS Appl. Mater. Interfaces*, 7 (2015) 9103–9109.
- [9] F.D. Ruz-Nuglo, L.J. Groven, 3-D printing and development of fluoropolymer based reactive inks, *Adv. Eng. Mater.*, 20 (2018) 1–8.
- [10] H. Wang, M. Rehwoldt, D.J. Kline, T. Wu, P. Wang, M.R. Zachariah, Comparison study of the ignition and combustion characteristics of directly-written Al/PVDF, Al/Viton and Al/THV composites, *Combust. Flame*, 201 (2019) 181–186.
- [11] C. Huang, G. Jian, J.B. De Lisio, H. Wang, M.R. Zachariah, Electrospray deposition of energetic polymer nanocomposites with high mass particle loadings: A prelude to 3D printing of rocket motors, *Adv. Eng. Mater.*, 17 (2015) 95–101.
- [12] T.J. Fleck, A.K. Murray, I.E. Gunduz, S.F. Son, G.T.C. Chiu, J.F. Rhoads, Additive manufacturing of multifunctional reactive materials, *Addit. Manuf.*, 17 (2017) 176–182.
- [13] J.A. Bencomo, S.T. Iacono, J. McCollum, 3D printing multifunctional fluorinated nanocomposites: tuning electroactivity, rheology and chemical reactivity, *J. Mater. Chem. A*, 6 (2018) 12308–12315.
- [14] M. Ponikvar-Svet, D.N. Zeiger, J.F. Liebman, Which halogen is the strongest oxidant? A study with systematics and surprises, *J. Struct. Chem.*, 26 (2015) 1621–1628.
- [15] S.K. Valluri, M. Schoenitz, E. Dreizin, Fluorine-containing oxidizers for metal fuels in energetic formulations, *Def. Technol.*, 15 (2019) 1–22.
- [16] J. Haslam, S.M.A. Whettem, The determination of fluorine in polytetrafluoroethylene, *J. Appl. Chem.*, 2 (1952) 339–344.

- [17] T.R. Sippel, S.F. Son, L.J. Groven, Altering reactivity of aluminum with selective inclusion of polytetrafluoroethylene through mechanical activation, *Propellants Explos. Pyrotech.*, 38 (2013) 286–295.
- [18] S. Gordon, B.J. McBride, Computer program for calculation of complex chemical equilibrium compositions and applications, Reference Publication 1311, (1994).
- [19] T. J. Fleck, T. D. Manship, S. F. Son, J. F. Rhoads, The effect of process parameters on the structural energetic properties of additively manufactured reactive structures, *J. Eng. Mater. Technol.*, 142 (2020) 041004.
- [20] Y. Cao, M. Liang, Z. Liu, Y. Wu, X. Xiong, C. Li, X. Wang, N. Jiang, J. Yu, C. Lin, Enhanced thermal conductivity for poly(vinylidene fluoride) composites with nano-carbon fillers, *RSC Adv.*, 6 (2016) 68357–68362.
- [21] W.J. Dixon, A.M. Mood, A method for obtaining and analyzing sensitivity data, *J. Am. Stat. Assoc.*, 43 (1948) 109–126.
- [22] M.L. Pantoya, S.W. Dean, The influence of alumina passivation on nano-Al/Teflon reactions, *Thermochim. Acta*, 493 (2009) 109–110.
- [23] J. McCollum, A.M. Morey, S.T. Iacono, Morphological and combustion study of interface effects in aluminum-poly(vinylidene fluoride) composites, *Mater. Des.*, 134 (2017) 64–708.
- [24] A.P. Chacko, Polymer composition and film having positive temperature coefficient, US Patent 20060043343A1, CTS Corporation (2006).
- [25] K.F. Warner, M.M. Sandstrom, G.W. Brown, D.L. Remmers, J.J. Phillips, T.J. Shelley, J.A. Reyes, P.C. Hsu, J.G. Reynolds, ABL and BAM friction analysis comparison, *Propellants Explos. Pyrotech.*, 40 (2015) 583–589.
- [26] P.W. Levy, The impact testing of explosives, *Nature*, 182 (1958) 37–39.

2. DYNAMIC X-RAY IMAGING OF ADDITIVELY MANUFACTURED REACTIVE COMPONENTS IN SOLID PROPELLANT

D. N. Collard, M. S. McClain, N. A. Rahman, N. H. Dorcy, T. R. Meyer, S. F. Son, “Dynamic X-ray imaging of additively manufactured reactive components in solid propellants,” *J. Propul. Power*, vol. 37, no. 3, pp. 362-368, 2021.

A variety of methods have been developed to enhance solid propellant burning rates, including adjusting oxidizer particle size, changing the formulation, modifying the propellant core geometry, and adding catalysts or wires. Fully consumable reactive wires embedded in propellant have been demonstrated to increase the burning rate by increasing the surface area; however, the observation of this effect has been limited to viewing via an intrusive window next to the wire. Here, we employ dynamic X-ray radiography to analyze the evolution of the internal burning profile of propellant embedded with additively manufactured reactive components. This avoids heat loss at the window and allows analysis of the three-dimensional volumetric consumption of strands with internal branching geometries. Printable reactive wires made of aluminum/polyvinylidene fluoride (Al/PVDF) were embedded as single wires, pitchforks, and U- and V-shape geometries. The nano-aluminum based formulation produced cone-shaped burning surfaces at 1 atm without the ejection of unburnt propellant, even for multiple wires burning in close proximity. Our results demonstrate a route to preferentially tailor the internal burning profile of propellants with embedded printable reactive wires and a dynamic X-ray imaging technique to qualitatively and quantitatively characterize the complex internal perforation development.

2.1 Introduction

In the past, significant efforts to tailor the burning rate of propellants involved a variety of methods, including changing the size of ammonium perchlorate (AP) oxidizer particles [1,2], employing novel oxidizers [3], and adding catalysts such as iron oxide or copper oxide particles and rods [4,5]. More recently, reactive wires [6], self-assembling and encapsulated nanoparticles [7], microwave-receptive absorbers [8] and thermal insulating additives [9,10] have been used to increase the burning rate via the effective burning surface area. Fabricating propellants to have

tailored burning surface areas, with printed reactive wires, for example, could make burning rate control via surface area modification far more viable.

Staples and inert wires embedded in propellants have long been used to tune burning rates over a limited range by increasing heat conduction from the flame into the propellant [11,12]. Preheating around the wires and staples leads to locally faster burning rates, which then increases the surface area at the interface and the overall mass burning rate. For example, embedding wires into a propellant transforms the burning surface from a relatively flat plane to a cone [11], [13–15]. Cones will also form in the presence of multiple burning rates with the fastest burning rate dominating [16]. In this case, the overall mass burning rate of the propellant is higher than an end burner configuration.

Reactive wires and consumable foils have been examined as alternatives to inert wires [6]. Self-alloying systems, such as Pyrofuze (an aluminum-palladium core-shell wire) [17] and nickel aluminum foils [18], were previously proposed for use in propellants, but not explored quantitatively as burning rate enhancers until implemented in Ref. [6]. A fully consumable reactive wire of pressed mechanically activated aluminum-polytetrafluoroethylene (MA Al-PTFE) was found to increase the specific impulse of the propellant and transform the burning surface area into a cone [6]. A windowed configuration was necessary for visible imaging, but restricted visualization of the reactive wire to two-dimensions. A window also affects the overall physics of the burning propellant since the wires are not embedded internally as it would be in application. To characterize the effect of reactive wires fully embedded in the propellant, other experimental methods are needed.

Multiple X-ray imaging techniques have been used to analyze defects in solid rocket motors [19, 20], examine throat erosion of nozzles [21], and measure the burning rate of propellant in strand burners and laboratory scale motors [22]. Recently, time-resolved synchrotron X-ray imaging has been used to investigate aluminum agglomeration in the optically opaque environment of a burning propellant [23]. In microCT, the stepped revolution of a sample through the beam over long times allows for a high-fidelity, multi-view reconstruction that can distinguish small differences in a material's density and absorptive properties. Time-resolved X-ray radiography can be achieved with a spatial resolution that is sufficient to investigate phase changes in reacting solid samples, but with limited ability to distinguish the smallest fluctuations in a sample with multiple, similar solid materials. As a complementary approach, phase contrast imaging [23] can be used to

resolve and enhance the visualization of interfaces within a multiphase sample, but volume data cannot be extracted. Furthermore, a large number of interfaces in the line of sight can lead to overlapping interference patterns and a limited the field of view.

In the current work, dynamic radiography with a high-power X-ray tube source is utilized for in-situ quantification of the local volumetric consumption rate and internal profile of burning propellants. This allows detailed evaluation of the burning characteristics of embedded reactive wires with varying composition and intricate geometries developed using additive manufacturing. The reactivity and printability of aluminum and polyvinylidene fluoride (Al/PVDF) [24,25] mixtures make this an ideal reactive to embed in propellant so that a range of branching geometries could be explored. The central aim of this study is to characterize the performance of printed reactive wires and to demonstrate the ability to preferentially tailor the burning profiles of AP composite propellant strands with X-ray radiography.

2.2 Methods

2.2.1 Reactive Wires

Printed reactive wires were fabricated from powders in a three-step process: 1) pelletization, 2) filament extrusion, and 3) printing with Fused Filament Fabrication (FFF). Extrudable reactive filaments were formulated with different types of aluminum. Nanoscale aluminum (nAl, 50 nm, Novacentrix Al-50-P) and 40 min high energy 70:30 wt.% mechanically-activated aluminum-polytetrafluoroethylene (MA Al-PTFE) (prepared as described in prior work in Ref. [26]), were combined with polyvinylidene fluoride (PVDF, Kynar 711). Aluminum was added to PVDF at an ideal stoichiometry of 20 wt.% active aluminum and 32.2 wt.% MA Al-PTFE. Filaments and printed reactive components were prepared as detailed in previous work [25]. Filaments were printed into a narrow and wide U-shape, two-pronged pitchfork with the prongs 3 mm and 7 mm apart, and V-shapes with double angles of 8° and 19° as shown in Figure 2.1. All of the depths were maintained at 1.5 mm to emulate the average diameter of unprinted filament.

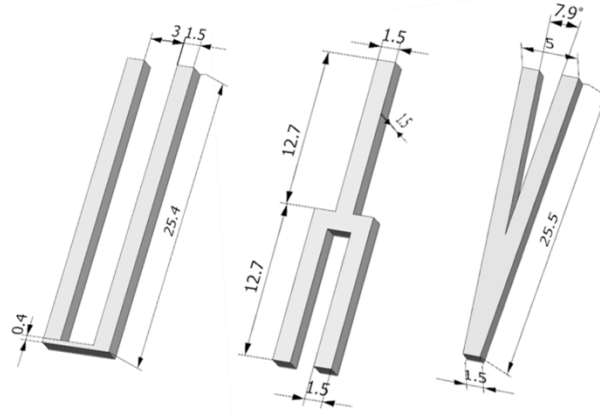


Figure 2.1. Narrow U-shape, pitchfork, and V-shape reactive wire geometries (units in mm).

Since the formulation of reactive wires was changed relative to previous work in order to achieve printability, straight reactive wires were chosen to provide a direct initial comparison to Ref. [6]. Pitchforks were chosen to examine how a burning front would split following one prong initially then splitting along the two prongs, while the V-shape allowed for the investigation of merging burning fronts. This allowed for the investigation of a range of separation to search for the dislodging of slivers and enhancement of burning rate. As such, it makes sense to orient the pitchfork so that the single prong then splits into two prongs and the V-shape has two prongs merge. The U-shape was chosen to ensure that the reactive wires stayed a specified distance apart when cast to give insight into a parallel multi-wire configuration. The orientation was chosen with the crossbar at the top to enable visual identification of the reactive location so that the ignition wire could be placed centrally. Narrow and wide geometries of each were chosen for two reasons. Firstly, the original camera and intensifier available had a smaller field of view (~ 7 mm) to achieve sufficient temporal and spatial resolution. Altering the camera setup to an intensified high speed camera allowed for the investigation of wider geometries, but again, a balance between the resolution and field of view limited the maximum size. Secondly, the enhancement of the burning rate and potential for slivering and sliver ejection is dependent on spatial positioning of the reactive wires, leading to the need to examine geometries with different distances between branches or prongs. The chosen reactive wires, printed geometries, and 20 gauge inert copper wires were embedded into 2.5 cm long propellant strands for combustion testing.

2.2.2 Propellant Formulation

Sections of filaments and printed geometries were cast into ammonium perchlorate (AP) composite propellant using a Teflon mold with a volume of 2.54 cm x 7.62 cm x 0.64 cm and three overflow holes on the top. Propellant strands consisted of 1.5 wt.% iron oxide (added as a catalyst and to increase contrast in X-ray imaging), 83.5 wt.% AP with a 4:1 coarse (60-130 μm , Firefox) to fine (20 μm , ATK) ratio. The binder formulation contained 76.68 wt.% hydroxyl-terminated polybutadiene (HTPB) (Rocket Motor Components), 15.05% isodecyl pelargonate (IDP) plasticizer (Rocket Motor Components), and 8.27% isophorone diisocyanate (IPDI) curing agent (Firefox). Batches of 35 g were prepared by initial hand mixing in a 475 mL polypropylene jar (McMaster Carr) until the AP was fully wetted. The jar was then placed into a resonant mixer (LABRAM Resodyn) and was mixed under vacuum for 3 min at 80 g's for three repetitions or until a large ball was formed. In Figure 2.2, half of the propellant was pressed in the mold and then the reactive components and copper wire were partially placed in the propellant. The rest of the propellant was then compressed on top until no more material squeezed through the overflow holes. The mold was then placed in an oven set at 60 °C for four days to cure.

Once cured, the propellant was removed from the mold and cut into 15 mm wide samples. Representative strands were examined with X-ray micro-computed tomography (Skyscan 1272 X-Ray MicroCT) to qualitatively inspect the reactive wire-propellant interface. Before combustion tests, the sides of the propellant strands were inhibited with nail polish to prevent burning along the sides of the propellant which can cause inverted coning.

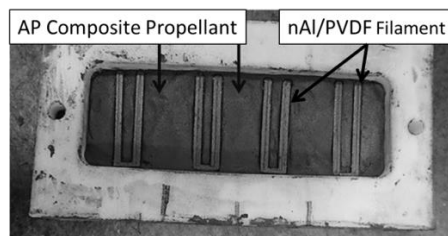


Figure 2.2. Four printed 5 mm wide nAl/PVDF U-shapes embedded in cast propellant.

2.2.3 X-ray Radiography

The propellant strands were adhered to a vertically variable stage using vacuum grease approximately 15 cm from the X-ray source and 15 cm from a phosphor scintillator plate. A

portable 0.3 mm polychromatic tungsten-based rotating anode X-ray source operated at an input voltage of 80 kV and current of 100 mA. Strands were subjected to an initial X-ray pass through for alignment purposes and exhibited no visually observable damage. The samples were then remotely ignited in open air at standard conditions with an electrically-heated 30 AWG Nichrome wire. The deflagrations were recorded with an intensified (Lambert Instruments HiCATT) high speed video camera (Photron SA-Z) at 1000 fps that was focused on a phosphor scintillator plate. Flexible sheets of opaque fabric were used to shield the intensifier and camera from the light of the flame and lead shielding encased the entire configuration to absorb errant X-rays (shielding is not shown in Figure 2.3 to elucidate the primary components of the experiment). The X-ray source could only run continuously for 6 s to avoid overheating, limiting the recording time. Tests were conducted in open atmosphere at standard conditions. Tests were not conducted at higher pressures as a custom pressure vessel specifically for the X-ray setup would be needed and is not yet available. A simple analysis is provided in the supplementary material, showing that sliver formation and ejection is not anticipated to be fundamentally different from atmospheric pressure to high-pressure burning.

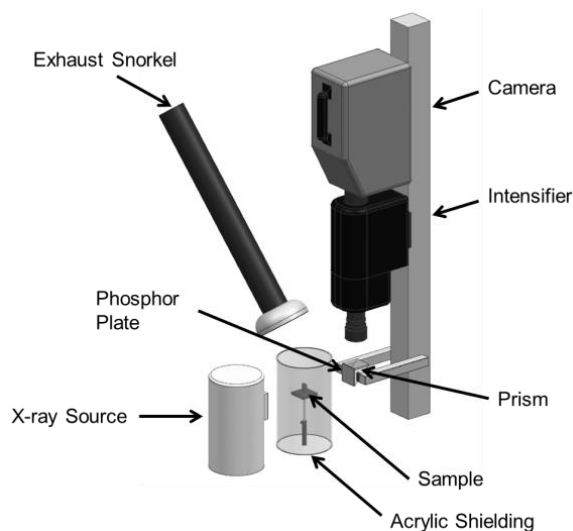


Figure 2.3. X-ray radiography configuration.

For improved visualization, contrast was enhanced only in the image progressions. The raw recorded images were used to create volumetric consumption traces by normalizing the background of each frame followed by processing with a MATLAB script designed to estimate

volume by extracting path length data. Images were reduced by averaging 5 x 5 pixel blocks to decrease the total number of calculations. All of the frames were corrected to the same brightness level by selecting an area identified as void of propellant throughout the test as the baseline brightness. A section of fully dense propellant from a baseline image was used to calculate an extinction coefficient using Beer's Law. Using the coefficient, the path length through each pixel block was calculated in each image. Pixel blocks were subsequently multiplied by the side lengths, which were determined using the x- and y-resolutions ranging from 30 to 42 $\mu\text{m}/\text{pixel}$. To reduce the appearance of noise in the volumetric consumption traces produced by the script, a moving average of 10 points was used. The volume traces were normalized against the initial volume of the sample.

2.3 Results

One way to measure the quality of propellant strands embedded with reactive components is to inspect for interconnected or concentrated porosity at interfaces. Strands with embedded reactive filaments and complex shapes were examined with X-ray micro-computed tomography (microCT) to inspect the interface between the Al/PVDF reactive wire and the surrounding propellant. Inadequate packing of the propellant around the embedded reactive materials can inadvertently lead to uncontrolled, and possibly violent, convective burning. As seen in Figure 2.4, the extruded filaments exhibited smoother surface than the printed parts as expected, but both adhered well to the propellant and showed no significant interfacial gaps from several viewpoints. In Figures 2.4-2.8, less dense material is represented by lighter colors.

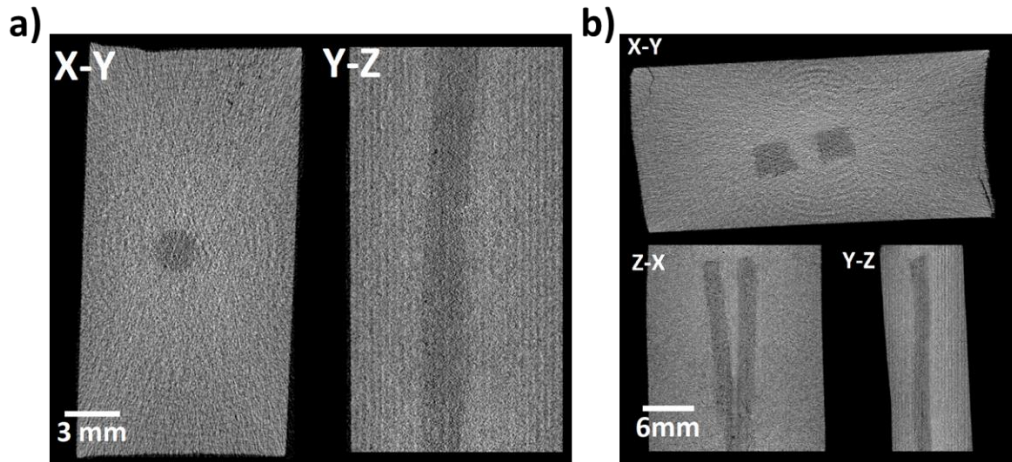


Figure 2.4. Cross-sections of microCT reconstructions of MA Al-PTFE/PVDF a) filament and b) printed V-shape strands cast in propellant.

Strands were imaged with a portable X-ray machine to eliminate the need for a windowed propellant configuration like that employed in previous work [6]. Individually, at atmospheric conditions, the burning rates are approximately 0.25 cm/s for the baseline propellant, 4 cm/s for nAl/PVDF filaments, and 2.4 cm/s for MA Al-PTFE/PVDF filaments. Figure 2.5a indicates that the baseline propellant burns in an expectedly planar manner. With an inert copper wire, as shown in Figure 2.5b, the heat from the reaction is conducted into the propellant, which promotes the reaction around the wire until a cone (half-angle of 8°) forms and the wire is ejected. In Ref. [6], the pressure dependency of the angle of coning directly around an inert copper wire was demonstrated, and at atmospheric pressure the half-angle is near 10° for the conditions considered using a window next to the wire. Until the inert wire is dislodged as the propellant burns out around it, the cone is not visibly discernable in the radiographs. The MA Al-PTFE/PVDF filament shown in Figure 2.5c does not burn faster relative to the surrounding propellant and no coning is observed. At higher pressure, this may not be the case depending on the pressure dependency of the filament which has not been measured. In Figure 2.5d, the nAl/PVDF filament burns faster than the surrounding propellant and coning is observed, which increases the overall burning surface area.

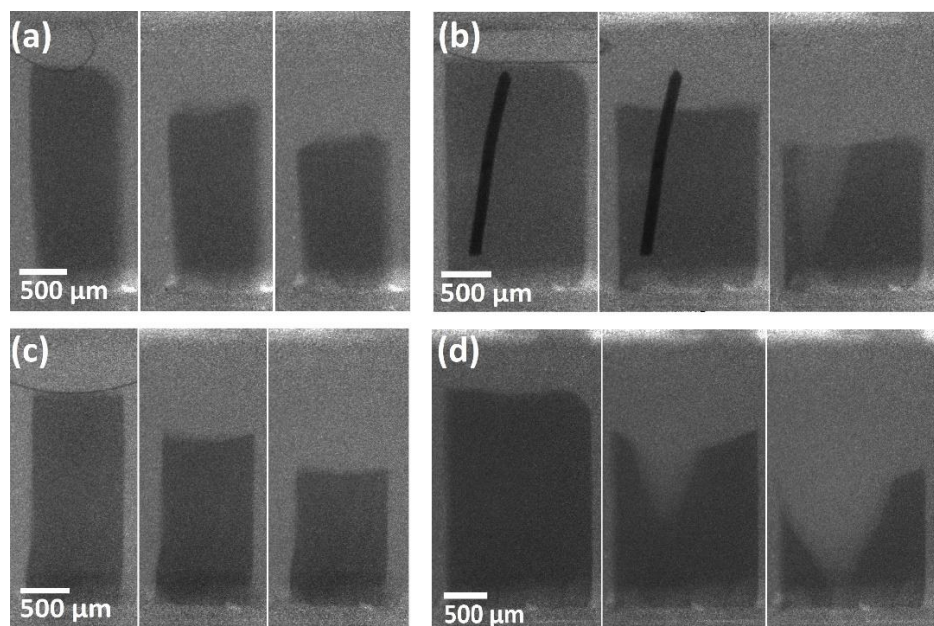


Figure 2.5. Radiographic progressions of a) baseline (no wires), b) inert copper wire, c) MA Al-PTFE/PVDF filament, and d) nAl/PVDF filament in propellant strands with frames every 3 s.

Since only the nAl/PVDF filaments demonstrated a faster propagation rate than the surrounding propellant, remaining strands with printed reactive geometries were made with nAl/PVDF. The density of the nAl/PVDF reactive wires were on average 1.770 g/cm^3 (89% TMD), and the propellant without the iron oxide additive had a density of approximately 1.526 g/cm^3 . The iron oxide additive comprised only 1.5 wt.%, resulting in a minimal effect on density with a theoretical maximum density of 1.659 g/cm^3 . In the radiographs shown in Figures 2.5-2.8, the density difference between the reactive wires and the propellant is not large enough to be detected by the X-ray radiography system. As the reactive wire is less than one-third of the path length through the sample, the effect on the absorption relative to a section of propellant alone is minimal. Furthermore, while density is a major factor in producing contrast, different materials exhibit different levels of X-ray absorption, which may contribute to the lack of contrast between the wire and propellant in the radiographs. However, the position of the parts can be determined in the propellant strand by following the evolution of the resulting cones (voids) that are easily observed. In Figure 2.6, it is shown that the burning follows the path of the reactive element from the single prong, across the crossbar, and down the set of double prongs. Since the propellant strands are rectangular in cross-section, the depth is not equal to the width. This leads to the cone of the burning surface to break out through the shorter dimension first. With the wider pitchfork, the cone

also breaks out on the left side of the propellant first, suggesting that the embedded component is off-center.

In all of the cases, despite the small separations between the branches of reactive material, the propellant exhibits individual coning along the reactive wires. Reactive wires near each other result in coalescing burning fronts. The slivering of propellant is of concern in rocket motors because ejection could lead to both energetic losses due to incomplete combustion and damaging affects downstream. Despite the development of some thin regions, most prominently in the wide V-shape in Figure 2.7 and both U-shapes in Figure 2.8, the slivers are not seen to detach in a frame-by-frame examination of the imaging, but are smoothly consumed as the burning cones merge.

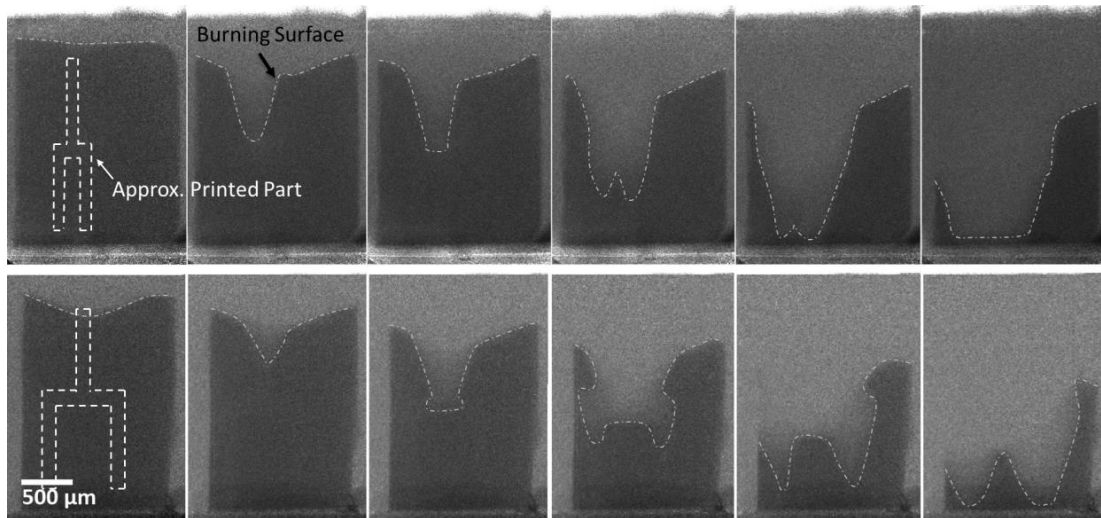


Figure 2.6. Radiographic progression of narrow and wide pitchforks with frames every 1.2 s.

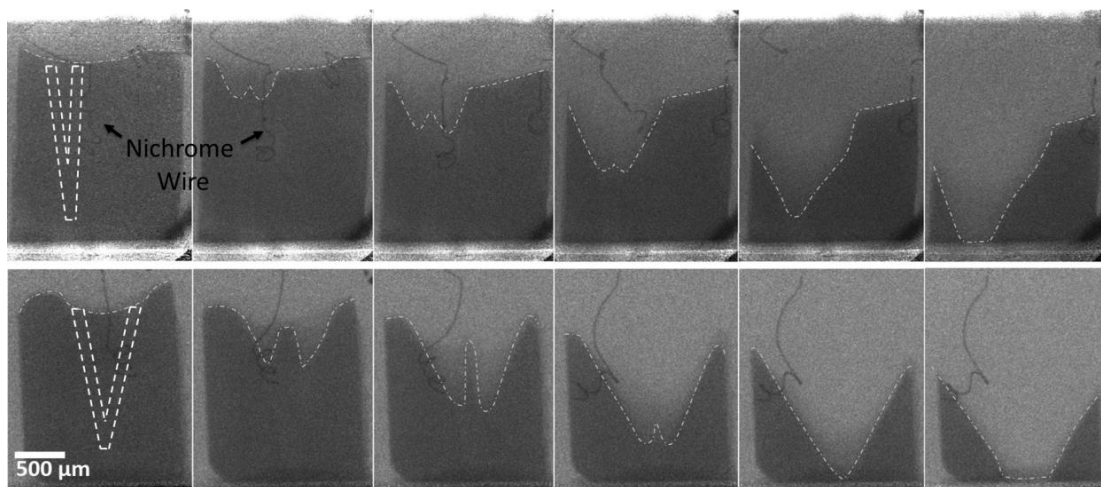


Figure 2.7. Radiographic progression of narrow and wide V-shapes with frames every 1.2 s.

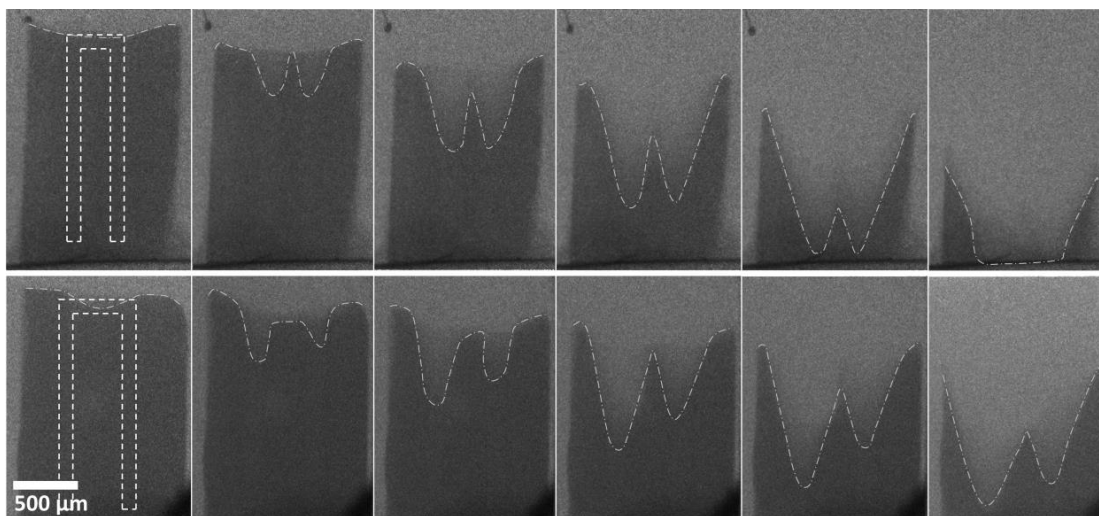


Figure 2.8. Radiographic progression of narrow and wide U-shapes with frames every 1.2 s.

Although tests were conducted with a single view, a volumetric consumption trace can be generated by calculating a path length from the intensity at each point. It is assumed that the density and the extinction coefficient is the same everywhere for the propellant and reactive wire. With this path length data, a volume at each frame can be estimated using the $\mu\text{m}/\text{pixel}$ resolution derived from a reference image. The calculation estimates the volume through the summation of rectangular prisms with depths equal to the path length.

The traces of the volumetric consumption of the tests are shown in Figure 2.9 with corresponding linear fits in Table 2.1. Linear regressions of volumetric consumption.

. The tests in Figure 2.9 were separated for ease of viewing by multiplying by the corresponding factors in the legends. The baseline mass burning rate was approximately 0.12 g/s. The baseline and MA Al-PTFE/PVDF filament exhibited similar consumption rates as expected since the MA Al-PTFE/PVDF filament did not burn fast enough relative to the surrounding propellant to change the burning front. The mass consumption rate of the other materials can be estimated by assuming a volume-weighted average density of $1.67 \text{ g}/\text{cm}^3$ in which approximately 95% by volume is AP composite propellant and 5% is nAl/PVDF. The propellant mass consumption rate with an embedded nAl/PVDF filament was approximately 0.25 g/s, or more than twice the rate of the baseline. In comparison, many typical solid catalysts, such as transition metal oxides, increase the burning rates by approximately 25-40% at atmospheric conditions [27, 28]. The increase in mass consumption rate of the nAl/PVDF filament is due to a combination of the faster burning of the filament itself to increase in surface area due to coning. Figure 2.9b and Figure 2.9d exhibit an

anomalous dip in some of the volume traces. The sudden decrease in volume is not due to sliver ejection, since the trace would not recover if unburnt material was ejected out of frame. Upon qualitative visual analysis, the dip corresponds to the escape followed by the reentry of the Nichrome ignition wire into the frame and light fluctuation due to the seepage of visible light from the flame, respectively. In Figure 2.9b, a change in volumetric consumption rate can be observed between a first stage, in which a single prong is burning, and a second stage, in which two prongs are burning simultaneously. As shown in Table 2.1, with the narrow pitchfork, the volumetric consumption rate of the double prongs was not quite twice as much as the single prong rate when the cones coalesced. The U-shapes and V-shapes behaved in a similar manner with the wider spacing between prongs exhibiting higher volumetric consumption rates than their narrow counterparts.

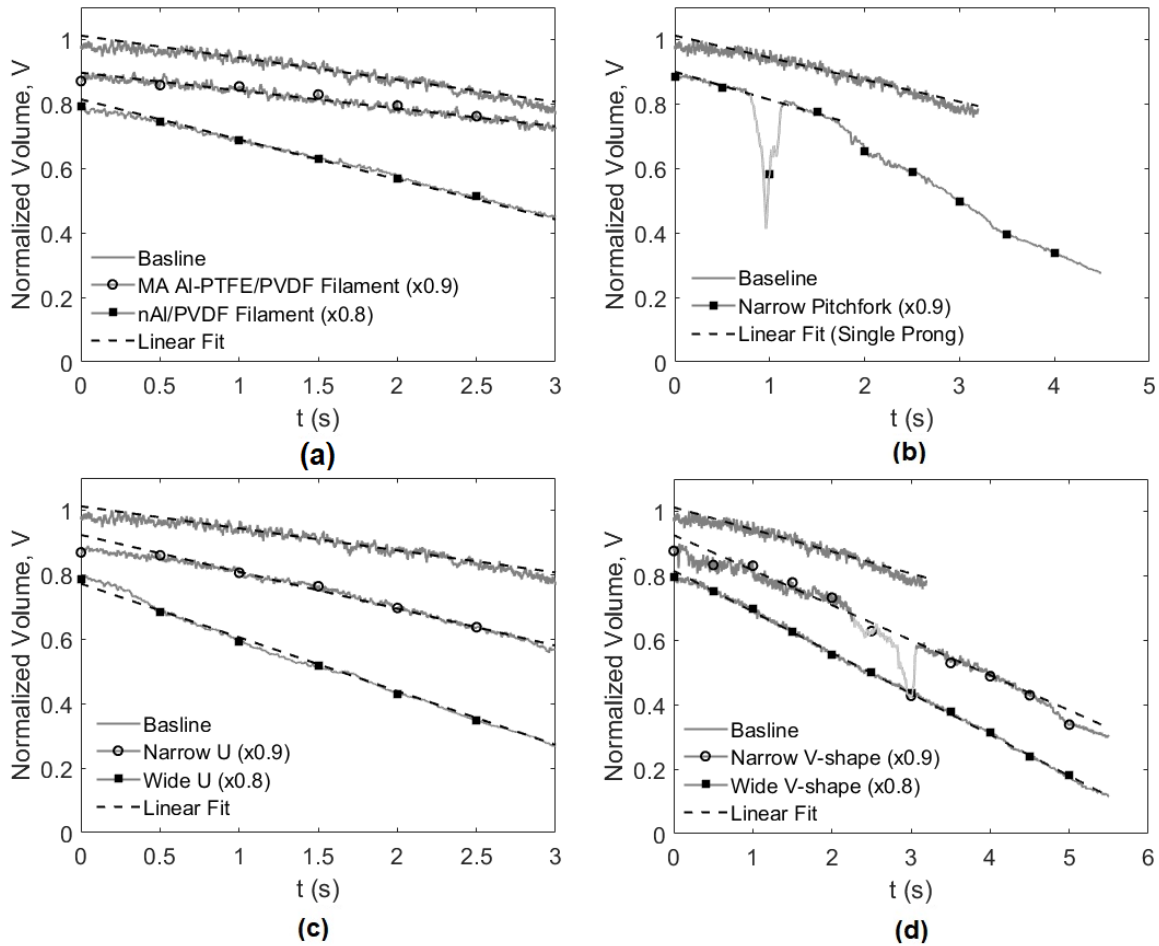


Figure 2.9. Volumetric consumption of (a) baseline and embedded filaments, (b) narrow pitchfork, (c) U-shapes, and (d) V-shapes with respective linear fits.

Table 2.1. Linear regressions of volumetric consumption.

Feature		Slope	R ²
Baseline		-0.07	0.95
MA	Al-PTFE/PVDF Filament	-0.06	0.99
nAl/PVDF Filament		-0.15	0.99
Narrow Pitchfork			
- Single Prong (0-1.75 s)		-0.10	0.98
- Double Prong (2.25-3 s)		-0.19	0.98
Narrow U-shape		-0.13	0.99
Wide U-shape		-0.21	0.99
Narrow V-shape		-0.12	0.98
Wide V-shape		-0.16	0.99

As the reaction front propagates along a reactive wire, the cone achieves equilibrium with a half-angle that can be described by Winch and Irvine [16] as

$$\theta = \text{asin}(r_b/r_{be}) \quad (1)$$

Once the propellant burning rate reaches equilibrium, the half-angle of the cone produced by the nAl/PVDF filament remains steady at 28°, which is similar to half-angle calculated in the model (27°). The surface area of the reaction front develops such that the effective burning rate is equivalent to the propagation rate of the reactive wire into the propellant. With two or more reactive wires embedded far enough apart to be thermally isolated from each other, each wire will develop a cone relative to its enhanced propagation rate. Once the burning has progressed such that the cones fully coalesce and no regions of the burning front are planar, the surface area becomes steady. This equilibrium surface area is such that the effective burning rate is equivalent to that of the higher burning rate of the reactive wires in the propellant. This could be readily determined for a single wire in a Crawford bomb. The effective burning rate of a propellant with multiple wires will nearly be this rate, assuming the spacing is sufficient that the nearby wires do not affect the leading burning fronts significantly. We note here that the increased surface area, resulting in a higher effective propagation rate, is analogous to turbulent combustion.

2.4 Conclusions

X-ray radiography was successfully applied to investigate inert and reactive wires embedded in propellant strands without the need for a window directly in contact with the propellant and wire. Reactive wires of nAl/PVDF successfully increased the propellant volumetric consumption rate through a combination of faster reacting material and the subsequent development of a cone-shaped burning front. MA Al-PTFE/PVDF filaments did not burn sufficiently fast to lead to coning at the given test conditions. Unlike their inert wire counterparts, reactive wires do not form large slag structures that greatly increase two-phase flow losses. Furthermore, the printable formulation of nAl/PVDF allowed for the testing of additively manufactured components. Some thin propellant structures were observed after the merging of multiple cones from two reactive wire branches; however, the thin slivers burned smoothly and did not eject at the conditions considered.

The reactive wires can be used to tailor the burning rates over a wide range by adjusting the stoichiometry of the Al/PVDF wire or constructing intricate geometries through additive manufacturing. The evolution of the burning surface can be captured by X-ray radiography, as demonstrated. Extending radiography to multiple views and testing at elevated pressure will enable the implementation and analysis of reactive elements under more realistic conditions and with more complex geometries, such as hooks, spirals, or branches in three dimensions.

2.5 Acknowledgments

We are grateful for the assistance of Tim Manship of Purdue University for designing the propellant mold. This work was supported by the National Science Foundation Graduate Research Fellowship Program Award No. DGE-1333468, AFOSR MURI Award No. FA9550-19-1-0008, and NASA Space Technology Research Fellowship Award No. 80NSSC17K0176.

2.6 References

- [1] Jain, S., Mehilal, Nandagopal, S., Singh, P. P., Radhakrishnan, K. K., and Bhattacharya, B., "Size and Shape of Ammonium Perchlorate and Their Influence on Properties," *Defense Science Journal*, Vol. 59, No.3, 2009, pp. 294–299. doi: 10.14429/dsj.59.1523
- [2] Isert, S., Hedman, T. D., Lucht, R. P., and Son, S. F., "Oxidizer Coarse-to-fine Ratio Effect on Microscale Flame Structure in a Bimodal Composite Propellant," *Combustion and Flame*, Vol. 36, No. 2, 2017, pp. 2283-2290. doi: 10.1016/j.combustflame.2015.10.015

- [3] Ali, A. N., Son, S. F., Hiskey, M. A., and Naud, D. L., "Novel High Nitrogen Propellant Use in Solid Fuel Micropropulsion," *Journal of Propulsion and Power*, Vol. 20, No. 1, 2004, pp. 120–126. doi: 10.2514/1.9238
- [4] Vargeese, A. A., "A Kinetic Investigation on the Mechanism and Activity of Copper Oxide Nanorods on the Thermal Decomposition of Propellants," *Combustion and Flame*, Vol. 165, Mar. 2016. pp. 354–360. doi: 10.1016/j.combustflame.2015.12.018
- [5] Hedman, T. D., Reese, D. A., Cho, K. Y., Groven, L. J., Lucht, R. P., and Son, S. F., "An Experimental Study of the Effects of Catalysts on an Ammonium Perchlorate Based Composite Propellant Using 5kHz PLIF," *Combustion and Flame*, Vol. 159, No. 4, 2012, pp. 1748–1758. doi: 10.1016/j.combustflame.2011.11.014
- [6] Isert, S., Lane, C. D., Gunduz, I. E., and Son, S. F., "Tailoring Burning Rates Using Reactive Wires in Composite Solid Rocket Propellants," *Proceedings of the Combustion Institute*, Vol. 36, No. 2, 2017, pp. 2283–2290. doi: 10.1016/j.proci.2016.06.141
- [7] Wang, H., Jacob, R. J., DeLisio, J. B., and Zachariah, M. R., "Assembly and Encapsulation of Aluminum NP's within AP/NC Matrix and Their Reactive Properties," *Combustion and Flame*, Vol. 180, 2017, pp. 175–183. doi: 10.1016/j.combustflame.2017.02.036
- [8] Barkley, S., Zhu, K., Lynch, J., Ballesteros, M., Michael, J., and Sippel, T., "Microwave-Supported Plasma Combustion Enhancement of Composite Solid Propellants Using Alkali Metal Dopants Multicomponent Droplet Vaporization and Wall Interactions," *54th AIAA Aerospace Science Meeting*, AIAA Paper 2016-0685, San Diego, 2016, pp. 1–9. doi: 10.2514/6.2016-0685
- [9] Wang, H., DeLisio, J. B., Holdren, S., Wu, T., Yang, Y., Hu, J., and Zachariah, M. R., "Mesoporous Silica Spheres Incorporated Aluminum/poly(vinylidene fluoride) for Enhanced Burning Propellants," *Advanced Engineering Materials*, Vol. 20, No. 2, 2018, pp. 1–7. doi: 10.1002/adem.201700547
- [10] Kline, D. J., Rehwoldt, M. C., Wang, H., Eckman, N. E., and Zachariah, M. R., "Why Does Adding a Poor Thermal Conductor Increase Propagation Rate in Solid Propellants?," *Applied Physics Letters*, Vol. 115, No. 114101, 2019. doi: 10.1063/1.5113612
- [11] Bakhman, N. N., and Lobanov, I. N., "Influence of the Diameter of the Heat-conducting Elements on Their Efficiency During the Combustion of Condensed Systems," *Combustion, Explosion, and Shock Wave*, Vol. 19, No. 1, 1983, pp. 42–46. doi: 10.1007/BF00790235
- [12] Caveny, L. H., "Influence of Embedded Metal Fibers on Solid-propellant Burning Rate," *Journal of Spacecraft and Rockets*, Vol. 4, No. 1, 1967, pp. 79–85. doi: 10.2514/3.28813
- [13] Rumbel, K. E., *Propellants Manufacture, Hazards, and Testing*, Advances in Chemistry, American Chemical Society, Washington DC, 1969, Chap. 3, 36–66. doi: 10.1021/ba-1969-0088.ch003

- [14] Kubota, N., Ichida, M., and Fujisawa, T., "Combustion Processes of Propellants with Embedded Metal Wires," *AIAA Journal*, Vol. 20, No. 1, 1982, pp. 116–121. doi: 10.2514/3.51056
- [15] Coats, D. E., French, J. C., Dunn, S. S., and Berker, D. R., "Improvements to the Solid Performance Program (SPP)," *39th AIAA/ASME/SAE/ASEE Joint Propulsion Conference and Exhibit*, AIAA Paper 2003-4504, Huntsville, 2003. doi: 10.2514/6.2003-4504
- [16] Winch, P. C., and Irvine, R. D., "Active Control of Solid Propellant Consumption Rate by Forced Cone Burning," *Journal of Propulsion and Power*, Vol. 4, No. 2, 1988, pp. 104–110. doi: 10.2514/3.23037
- [17] Irvine, R. D., and Winch, P. C., "A Solid Propellant Charge Design with Negative Effective Pressure Exponent Using Forced Cone Burning," Weapons Systems Research Lab WSRL-0469- TR, 1986.
- [18] Rice, M. L., Burton, J. M., and Shaver, R. G., The Susquehanna Corporation, Annandale, Alexandria, Burke, VA, U.S. Patent Application for a "Propellant Grains," Docket No. 3,509,822, filed 9 Jun. 1960.
- [19] Ghose, B., Mall, V. P., Dhare, B. D., and Kankane, D. K., "Digital Radiography of Solid Rocket Propellant with 4-MEV Linac X-Ray Using Computer Radiography (CR) System," *Proceedings of the National Seminar & Exhibition on Non-Destructive Evaluation*, NDE, Pune, India, 2011, pp. 311–313.
- [20] Remakanthan, S., Gunasekaran, R., Thomas, C., and Thomas, C. R., "Estimation of Defects In Solid Rocket Motors Using X-Ray Radiography," *Proceedings of the National Seminar & Exhibition on Non-Destructive Evaluation*, NDE, Vol. 20, No. 6, Pune, India, 2014.
- [21] Colbaugh, L., "Indirect and Direct Methods for Measuring a Dynamic Throat Diameter in a Solid Rocket Motor," Masters Thesis, Mechanical and Aerospace Engineering Dept., Univ. of Alabama-Huntsville, Huntsville, Alabama, 2014.
- [22] Denny, M. D., "Measurement of Solid Rocket Propellant Burning Rate Using X-Ray Imaging," Ph.D. Thesis, Mechanical and Aerospace Engineering Dept., Univ. of Alabama-Huntsville, Huntsville, Alabama, 2015.
- [23] Kalman, J., Demko, A. R., Varghese, B., Matusik, K. E., and Kastengren, A. L., "Synchrotron-based Measurement of Aluminum Agglomerates at Motor Conditions," *Combustion and Flame*, Vol. 196, Oct. 2018, pp. 144-146. doi: 10.1016/j.combustflame.2018.06.013
- [24] Fleck, T. J., Murray, A. K., Gunduz, I. E., Son, S. F., Chiu, G. T.-C., and Rhoads, J. F., "Additive Manufacturing of Multifunctional Reactive Materials," *Additive Manufacturing*, Vol. 17, Oct. 2017, pp. 176–182. doi: 10.1016/j.addma.2017.08.008

- [25] Collard, D. N., McClain, M., Fleck, T., Rahman, N., Rhoads, J., Meyer, T., and Son, S., "Solid Propellant with Embedded Additively Manufactured Reactive Components", *AIAA Propulsion and Energy Forum*, AIAA Paper 2019-4443, Indianapolis, 2019. doi: 10.2514/6.2019-4443
- [26] Sippel, T. R., Son, S. F., and Groven, L. J., "Altering Reactivity of Aluminum with Selective Inclusion of Polytetrafluoroethylene through Mechanical Activation," *Propellants, Explosives, Pyrotechnics*, Vol. 38, No. 2, 2013, pp. 286–295. doi: 10.1002/prep.201200102
- [27] Kishore, K., Pai Verneker, V. R., and Sunitha, M. R., "Effect of Catalyst Concentration on Burning Rate of Composite Solid Propellants," *AIAA Journal*, Vol. 15, No. 11, 1977, pp. 1649–1651. doi: 10.2514/3.7466
- [28] Gilbert, P. D., Zaseck, C. R., Nazario, R. L. and Son, S. F., "An Investigation of Novel Metal Complexes as Composite Propellant Burn Rate Modifiers," *44th AIAA/ASME/SAE/ASEE Joint Propulsion Conference and Exhibit*, AIAA Paper 2008-5260, Hartford, Connecticut, 2008. doi: 10.2514/6.2008-5260

3. EXTRUSION OF AP COMPOSITE PROPELLANT WITH SELF-ALIGNED REACTIVE FIBERS

D. N. Collard, J. A. Curtiss, M. Gomez, H. A. Bilbo J. F. Rhoads, T. R. Meyer, S. F. Son, “Extrusion of AP composite propellant with self-aligned reactive fibers,” *AIAA Propulsion and Energy Forum and Exposition*, Virtual, August 9-11, 2021.

Consumable reactive wires embedded in solid propellant have been previously demonstrated to increase the burning rate through a geometric effect that increases surface area. However, branching and complex geometrical reactive components within propellant grains remain difficult to fabricate as distinct, dissimilar materials often require multiple techniques for manufacture. In this study, instead, of utilizing multiple techniques, reactive fibers are mixed into an AP composite propellant matrix and extruded in a prescribed direction, resulting in the self-alignment of the fibers within the flow. The effect of aspect ratio (AR) and orientation of fibers on the effective burning rate are investigated with visible imaging and X-ray tomography. Fibers of higher AR and oriented perpendicular relative to the burning front (referred to as “vertical orientation” in this paper) increased the effective burning rate of AP composite propellant the most.

3.1 Introduction

Many methods to improve the burning rate of solid composite propellant systems have been studied ranging from the utilization of fuel and oxidizer particle size effects [1–6], the implementation of novel oxidizers [7], the inclusion of metal particles and composites [8–13], catalysis with metal oxides [14–15], and the addition of wires, staples, and absorbers [16–18]. However, the catalysis and burning rate accelerants are not the only contributors to increased burning rate. Extremely fast decomposition or combustion of fast-burning additives within the composite propellant matrix leads to geometric effects, often called cratering or coning [16, 19–22]. Additive manufacturing [23–25] and reactive wires [16, 26] have been used to further utilize these geometric effects. However, while additive manufacturing (AM) lends itself to the construction of unique geometric shapes inaccessible to traditional techniques, many AM methods have difficulties with high volume prints [27–29]. In addition, additive manufacturing can be a relatively labor-intensive process compared to traditional manufacturing techniques. It requires a

uniform feedstock and significant time investment to achieve consistent quality [30]. For example, to print a cylinder with a diameter and height of 1 cm with a reactive filament of Al/PVDF using the fused-filament fabrication (FFF) method described in Refs. [31–32] can take more than 20 min of direct print time to manufacture. Furthermore, the crossover of multiple printing techniques for dissimilar materials can lead to other challenges, one of the most prominent of which concerns adhesion. Unintentional gaps in energetic materials applications could lead to convective burning and catastrophic results.

Reactive wires have been demonstrated to enhance the burning rate of ammonium perchlorate (AP) composite propellant by increasing the burning surface area with a coning effect [16, 26]. In previous work [26], the reactive wires were additively manufactured and the propellant was cast around the wires. To fully print an AP composite propellant strand with an embedded Al/PVDF reactive wire, two different additive techniques are needed. The reactive wires would be printed via melt-extrusion while the AP composite propellant would be printed with a direct-write system known as vibration-assisted printing (VAP) [23–24]. Printing dissimilar materials, especially materials with distinct properties that require different printing techniques, comes attendant with a number of challenges.

Another approach to additively manufacture a reactive core compatible with the surrounding solid propellant is to use the propellant itself as a carrier for the reactive component. Fast-burning inclusions with significant AR could act as small reactive wires and increase the effective burning rate of the propellant. This could circumvent the adhesion difficulties that come with using multiple printing techniques and the vastly different materials between the core and the main body of the propellant. Additionally, transitioning the reactive wires to an extrusion-based direct write technique can vastly improve the fabrication speed depending on the size of the syringe and nozzle. Furthermore, asymmetric particles have been shown to self-align with the direction of the flow of bulk material [33–34]. This could open a potential facet of tailorability governed by the extrusion orientation of the reactive elements within a propellant matrix.

In this study, fast-burning nAl/PVDF reactive fibers were extruded with uncured AP composite propellant in a specified path to self-align fibers with the direction of the extrusion. The cured propellant was analyzed with visible imaging and X-ray tomography to quantify the effect of AR and orientation of reactive fibers on the burning rate of AP composite propellant strands.

3.2 Materials and Methods

Filaments of reactive nAl/PVDF material were prepared as described in previous work [32]. The filament was extruded continuously through a fused filament fabrication (FFF) print head with a heated nozzle of 0.5 mm diameter at 240 °C. This led to a new filament diameter of approximately 0.85 mm throughout due to die swell after exiting the nozzle. The resulting filament was chopped into reactive fibers with length-to-diameter AR of 1, 3, 5, and 7 as shown in Figure 3.1.

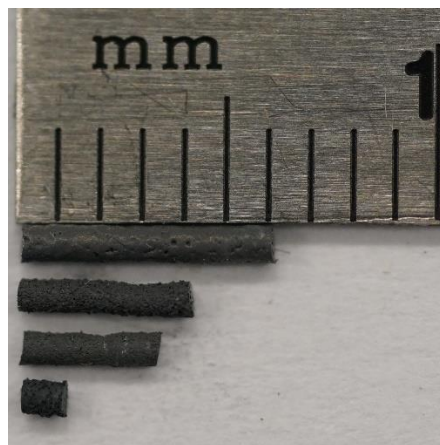


Figure 3.1. Reactive Al/PVDF fibers of 1, 3, 5, 7 AR.

Solid composite propellant with reactive fibers of a given ratio was formulated with 65 wt.% AP at a 4:1 coarse (60-130 μm , Firefox) to fine (20 μm , ATK) ratio, 10 wt.% reactive fibers, and 25 wt.% binder. The binder consisted of 19.08 wt.% R45 hydroxyl-terminated polybutadiene (RCS Rocket Motor Components, Inc.), 3.76 wt.% isodecyl pelargonate plasticizer (RCS Rocket Motor Components, Inc.), and 2.16 wt.% isophorone diisocyanate curative (Firefox). The baseline propellant consisted of 75 wt.% AP with 25 wt.% binder with no reactive fibers.

After an initial mix by hand, the propellant was placed in an acoustic mixer (LABRAM Resodyn) for two cycles of 3 min at 80 g to ensure adequate mixing. Baseline propellant and propellant with a fiber AR of 5 or less was packed into a pressure driven 30-cc syringe with a nozzle diameter of 4 mm. The syringe was attached to a Hyrel 3D printer via a printed ABS bracket. Since reactive fibers in the propellant self-align with the direction of the extrusion due to particle flow out of the nozzle, the build plate movement was prescribed with the longest dimension

lengthwise for all of the samples as in Figure 3.2. Propellant was extruded onto a glass microscope slide in nine lengthwise passes for three layers (Figure 3.2) to build a strand with approximate dimensions of 45 mm x 65 mm x 10 mm. To test the effect of fiber AR, strands with fibers of AR ranging from 1 to 7 were extruded with fibers aligned in a vertical orientation (fibers perpendicular to the burning front). To test the effect of fiber alignment, propellant blocks with 5 AR fibers were cut in a vertical, horizontal, and 45° orientation.

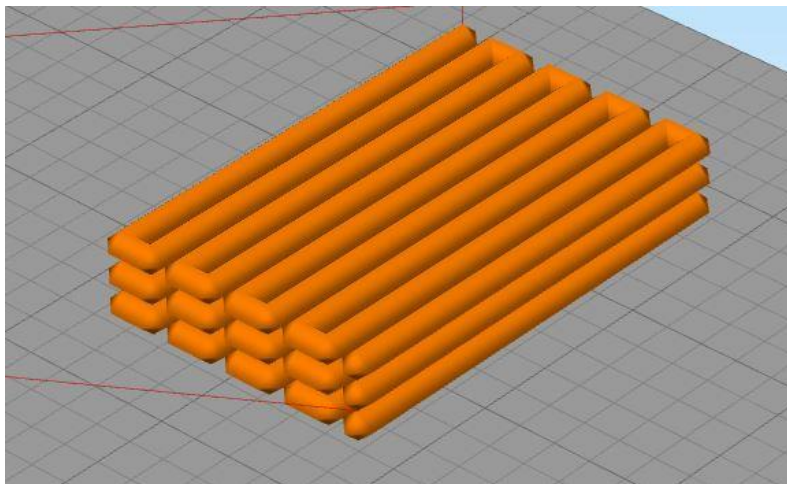


Figure 3.2. Preview schematic of extrusion path.

The formulation with fibers of an AR greater than 5 had difficulties being extruded from the standard 4 mm diameter nozzle of the syringe. The nozzle was opened further to 10 mm when extruding a fiber AR of 7, and the formulation was extruded in a single pass two layers high with a layer height of 5 mm to create an equivalent strand to the lower AR. The driving pressure was lowered to compensate for the differences in the outlet diameter and adjust the flowrate to an adequate level for the build plate movement. All of the samples were cured after extrusion in an oven at 60 °C for 4 days.

Once cured, 5 mm of each end of the propellant strands were cut away to eliminate the concentration of non-aligned strands due to startup and vertical travel moves between layers. The remaining cured propellant was cut into test samples of approximately 5 mm x 5 mm x 20 mm. The middle portion of a length of nichrome wire was coiled into a loop with a diameter of approximately 1 mm then adhered to the propellant strand with nitrocellulose lacquer to prevent movement during sample loading. The sides of the sample were inhibited with nail polish. Strands

were burned in a pressurized strand burner under nitrogen and recorded by a high-speed camera (Vision Research Phantom v10). Videos of the combustion were processed manually. Due to the reactive fibers, the burning surface was uneven. To account for the uneven burning surface and to get an average of the flame front progression, the burning surface position was measured along three equally spaced lines drawn perpendicular to the burning front. The flame front progression along these lines were then averaged and reported as the resulting propagation rate.

Propellant strands were examined with dual-view dynamic X-ray imaging (Figure 3.3) to examine the burning reactive wire strands in-situ. The two X-ray paths passed orthogonally through the sample onto two phosphor scintillator plates. The resulting visible images were redirected upwards with a prism and captured with intensified (Lambert Instruments HiCATT and LaVision UV IRO) high-speed cameras (Vision Research Phantom v2012). The propellant strands were adhered with vacuum grease to a three-axis variable stage approximately 5.5 in from the X-ray sources and 2 in from each phosphor plate. The samples were remotely ignited with an electrically-heated 30 AWG Nichrome resistive wire and the deflagrations were recorded at 1000 fps. Deflagration tests were conducted at standard atmospheric conditions. The X-ray sources consisted of two portable 0.6 mm polychromatic tungsten-based rotating anodes operated at an input voltage of 40 kV and current of 100 mA. The X-ray sources restricted the recording time to a maximum of 5 s to avoid overheating. Polycarbonate plates with a thickness of 0.25 in were lined with flexible sheets of opaque fabric to protect the cameras from the light of the flame, heat, and chemical byproducts. The entire X-ray configuration was contained in lead shielding to absorb errant radiation. Tomographic reconstruction was conducted on images pre-processed to normalize the background and decrease speckling.

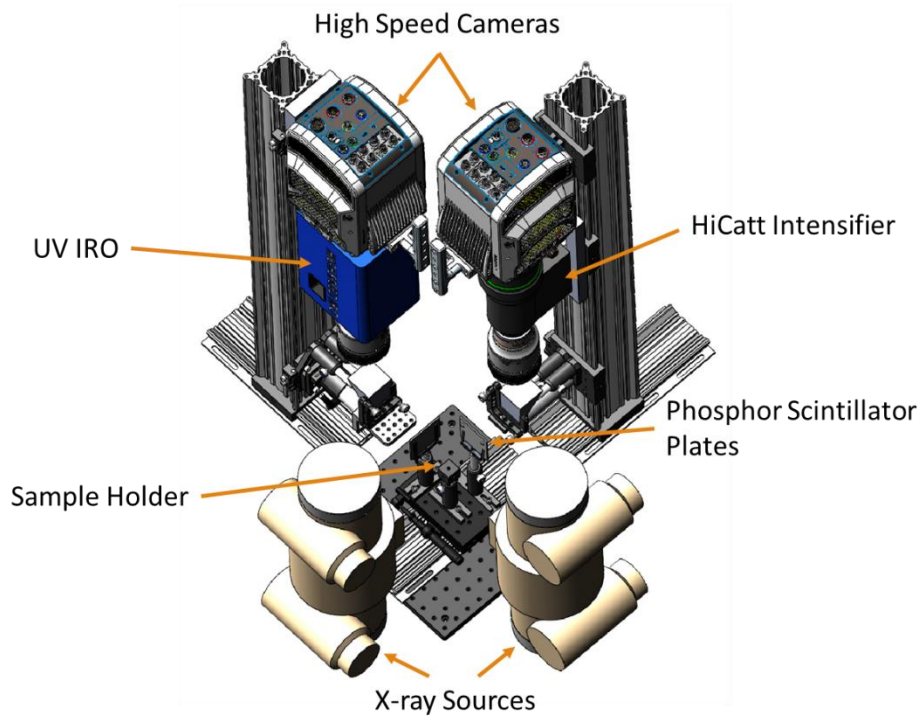


Figure 3.3. Schematic of dual-view dynamic X-ray imaging system.

3.3 Results and Discussion

Given that the propellant cures semi-transparent, as seen in Figure 3.4, the orientation of fibers can be quantified off of the prescribed extrusion path in both the vertical (YZ-plane) alignment with glass substrate and horizontal (XZ-plane) alignment. The average deviation of angle (Table 3.1) in the YZ-plane is lower than that of the deviation in the XZ-plane. A contributor to this difference may be the thermo-cured binder. As the binder takes time in elevated temperatures to cure, some sagging occurs as the weight of the top layers press down on the bottom layers. Sagging can press the reactive fibers out of alignment and lead to material pushing out the edges of the sample. Replacing the thermal-set HTPB binder with a UV curable polymer [25] could potentially reduce displacement due to sagging as the strand could be solidified more quickly or in a layer-by-layer fashion.

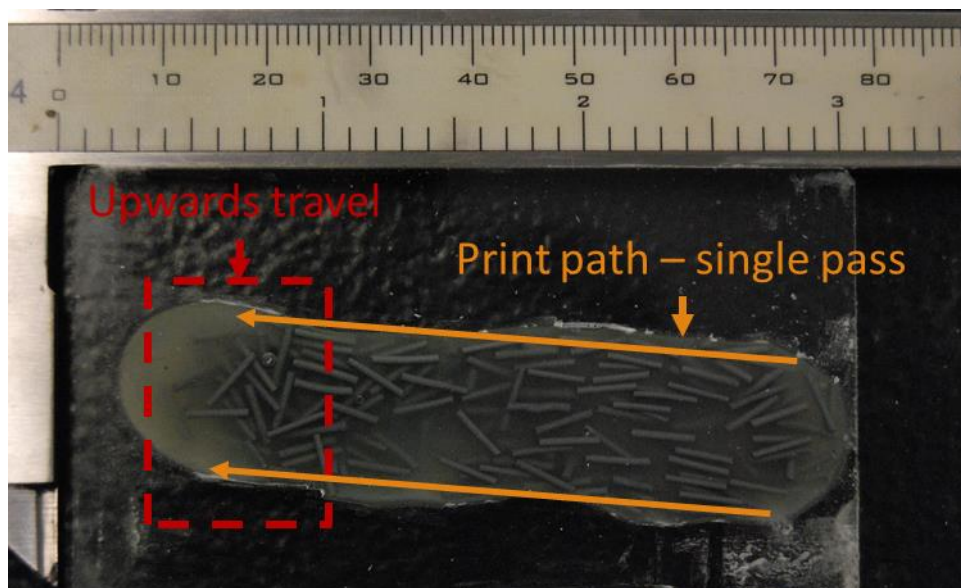


Figure 3.4. Underside of a cured extruded sample with 7 AR fibers.

Table 3.1. Average angle deviation from Z-axis aligned with the extrusion direction and substrate.

Absolute Angle	Average Angle (°)	Standard Deviation (°)	Fibers Measured
YZ-Plane	4.6	4.5	60
XZ-Plane	7.8	8.0	266

In both planes, a small number of fibers were seen orthogonal to the extrusion, breaking the general self-alignment and increasing the standard deviation off-axis. These fibers may be caught sideways in the extruder nozzle. If too many fibers are caught sideways, the nozzle clogged, resulting in a failed extrusion. Lips at the end of the nozzle led to increased instances of clogging and dewetting of both the fibers and AP particles and had to be removed. Larger AR fibers also required a larger nozzle opening to mitigate the clogging. For example, the 7 AR fibers were unable to complete a full extrusion with the initial selected nozzle size of 4 mm. To sustain extrusion with 7 AR fibers, the nozzle was drilled out to 10 mm to eliminate any lips within the syringe. Sufficient flow through the wider nozzle continued to exhibit self-alignment of fibers in the composite propellant matrix.

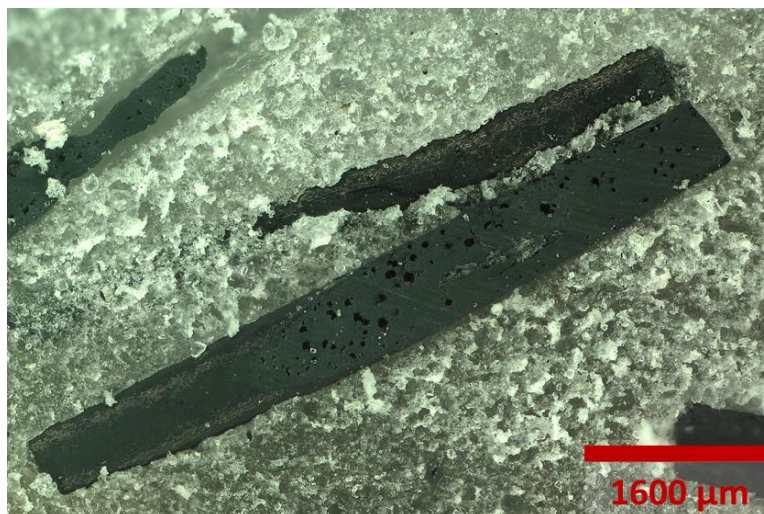


Figure 3.5. Microscopic images of a slice of propellant with 7 AR fibers.

The composite propellant showed good infill surrounding the reactive fibers (Figure 3.5) with no gaps between the fibers and surrounding propellant matrix. The gap in the upper left of Figure 3.5 was due to the razor blade dragging the fiber through the propellant as the sample was sliced and is consistent with the cut direction. The fibers have an inherent porosity of approximately 10%, similar to previously quantified porosity in Ref. [32]. Through Archimedes principle, the average density of the entire propellant samples with 10 wt.% reactive fibers were 1.48 g/cm³ (97.5% TMD) and baseline no fiber samples were 1.49 g/cm³ (98.3% TMD), indicating few gaps, bubbles, or extrusion defects.

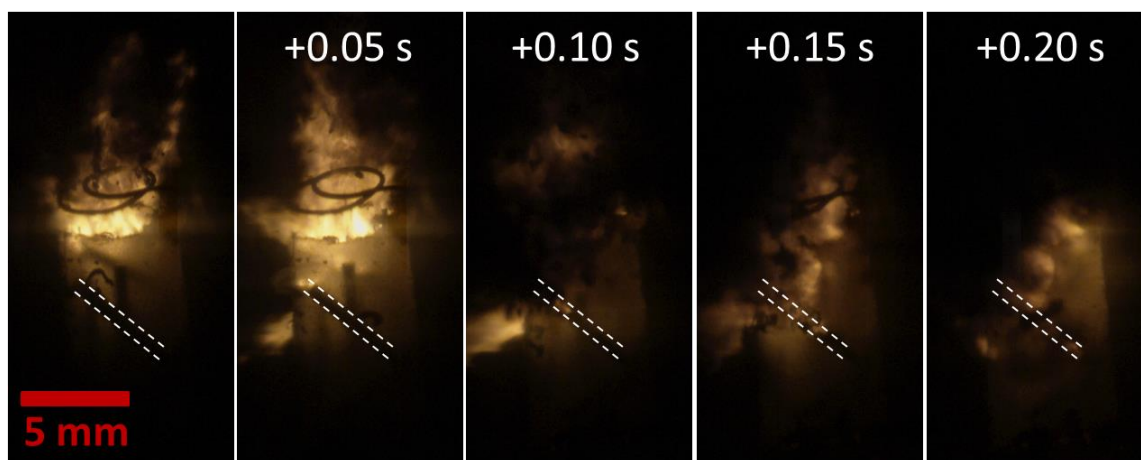


Figure 3.6. A failed 45° 5 AR propellant deflagration test with nail polish as an inhibitor.

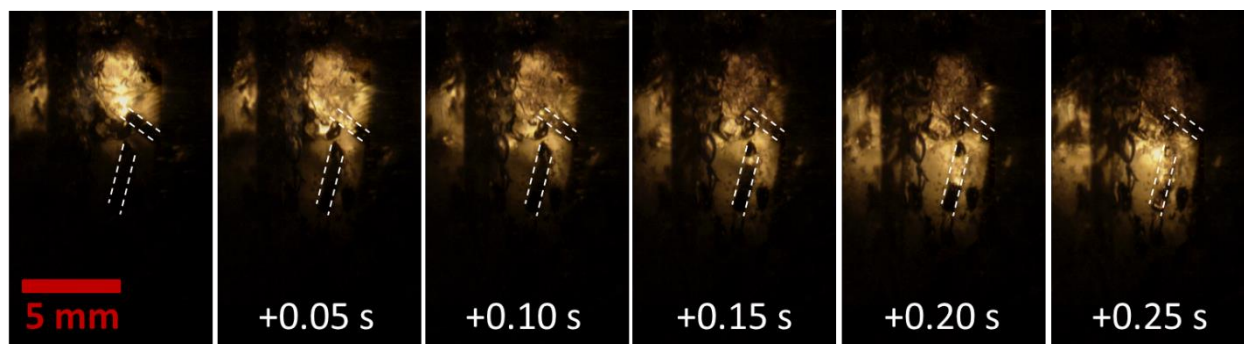


Figure 3.7. A 45° 5 AR propellant deflagration test with sample encased in epoxy in a cuvette cell.

Reactive fibers with orientations off vertical resulted in soot from the fibers frequently breaking out of the side of the strand through the nail polish inhibitor and obstructing view of the burning surface as seen in Figure 3.6. Dashed lines in Figures 3.6 and 3.7 highlight the positions of reactive fibers near the surface closest to the propellant, which are easily observed during reaction of the sample. The resulting soot obstructed the view of the burning surface and hindered the measurement of burning rate. To resolve this issue, propellant strands were cast into acrylic cuvette cells filled with clear 5 min epoxy. On average the samples were approximately 5.5 mm in width and the configuration showed little effect in the burning rate (Figures 3.8 and 3.9) as demonstrated by the repeated samples of baseline AP and 5 AR fibers with vertical alignment.

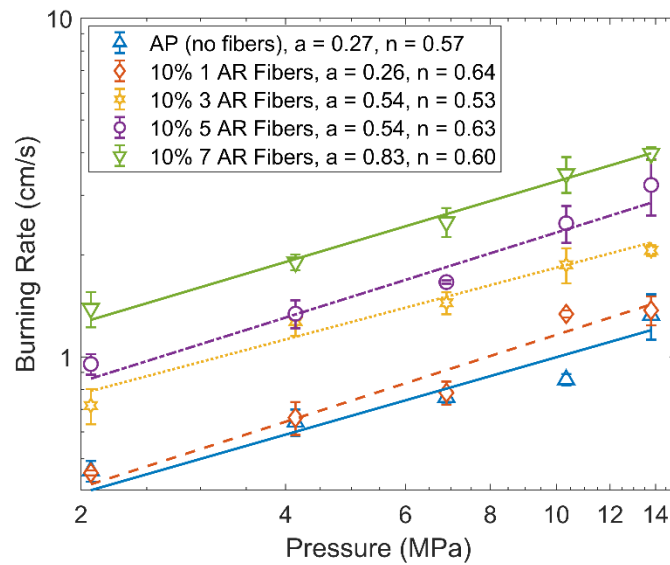


Figure 3.8. AP propellant burning rates with fibers of various aspect ratios oriented vertically within the strand.

Given that the burning rate of the reactive fibers was significantly higher than that of the surrounding propellant, the uneven surface made burning rate extraction difficult. An average burning rate of the propellant sample was determined by selecting the burning surface at five equally spaced axes along the length of the propellant strand. This was replicated with three samples at each pressure. The average burning rates across the three samples are plotted (Figures 3.8 and 3.9) with the error bars representing the standard deviation between the three samples. The average burning rates were fit with a power regression with a being the pre-exponential factor and n the power exponent.

As the reactive fiber AR increased, the effective burning rate of the propellant strands increased, as seen in Figure 3.8. The increased fiber length may have resulted in an enhanced cone burning as the reaction proceeds deeper into the strand. Larger cones in the propellant surface produces a geometric effect by opening more surface area to the reaction front, effectively increasing the burning rate. If the fibers are too short, the cone has little time to develop, significantly reducing the geometric enhancement of the deflagration as seen in the 1 AR fibers. The 1 AR fibers show a smaller burning rate improvement over the baseline propellant than the higher AR, acting more as a metallized particle additive than a surface enhancer.

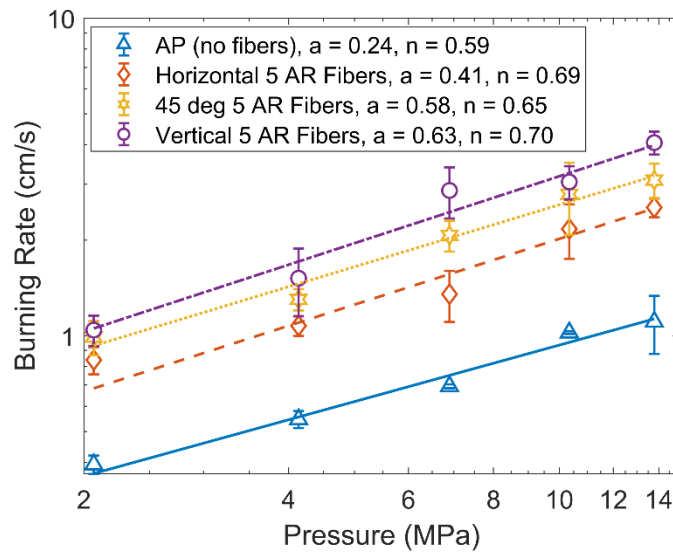


Figure 3.9. AP propellant burning rates with 5 AR fibers of various orientation within the strand.

The orientation of the fibers also plays a significant role in the enhancement of the effective burning rate (Figure 3.9) with fibers oriented vertically (perpendicular to the reaction front) exhibiting the greatest enhancement. This supports the geometric effect as the primary means improving the effective burning rate, as fibers oriented horizontally increase the surface area less than vertical fibers.

The development of cones in the surface are difficult to examine with visible imaging as the fibers closest to the edges of the strands are the only fully visible fibers. To analyze and quantify effects of the fiber in-situ, the internal propellant must be imaged. However, multiple fibers could be arranged within the X-ray path, one behind the other, such that a single plane of intensity data was not sufficient to visualize and quantify the burning effects. X-ray imaging with two views allowed the analysis of reactive wires throughout the propellant matrix with tomographic reconstruction.

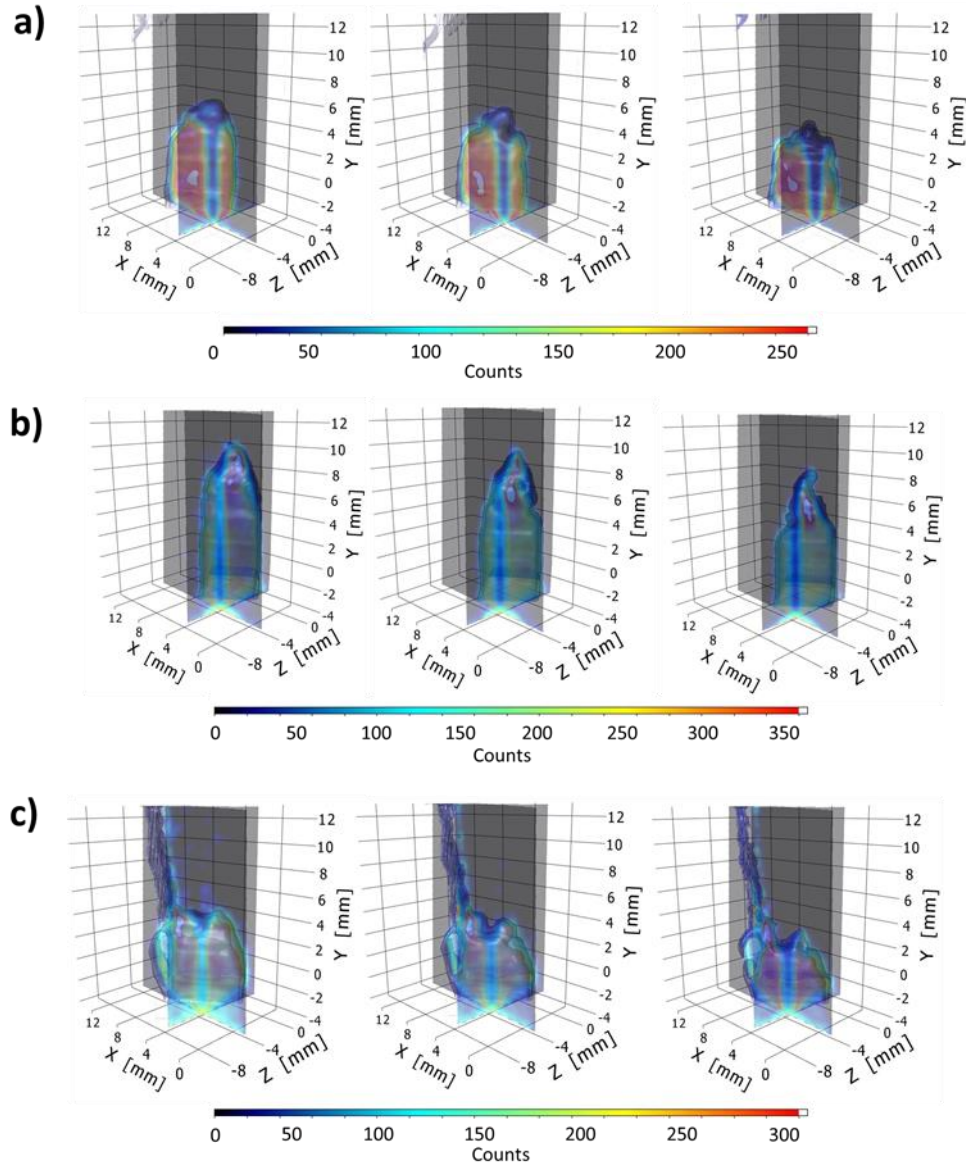


Figure 3.10. Tomographic reconstruction of in-situ dual-view X-ray of reacting a) vertical, b) 45°, c) horizontal 5 AR propellant strand with frames 0.25 s apart.

The tomographic reconstructions in Figure 3.10 show the different evolutions of the burning surface given the orientation of the fibers within the propellant. The vertically oriented fibers (Figure 3.10a) created simultaneous divots in the burning surface, making the surface appear more uniform during steady burning as the craters merged during reaction. Fibers with a 45° orientation (Figure 3.10b) created an oscillator appearance of the surface, as the craters created by the fibers burned at a diagonal, creating a sequence of crater formation that did not uniformly

merge. The horizontally oriented fibers (Figure 3.10c) created lengthy craters across the surface. A vertical crater with a longer component in the Y-axis (with respects to Figure 3.10) provides the most increase in the burning surface area with the largest coning. An angled crater also increases the surface area but given that one side of the cone-shaped crater has partially burned away, the increase is smaller than that of vertical craters. A shallow crater, as formed with a horizontal fiber, increases the surface area the least.

3.4 Conclusions

Fast burning reactive fibers in propellants are a viable additive to significantly increase the effective burning rate of solid propellants. Reactive fibers of various AR and alignments were fabricated by extruding along a prescribed path. With sufficient flow, the resultant particle flows self-aligned the fibers with the extrusion direction. As the AR of the reactive component increased, the effective burning rate increased, primarily due to enhanced geometric effects that opened more surface area to the burning front. Orientation of the fibers within the propellant matrix affected the effective burning rate with fibers oriented perpendicular to the initial burning surface resulting in the highest improvement. Reacting propellant strands were visualized with X-ray tomography, capturing the different surface area evolution due to the orientation of the faster reacting fibers.

3.5 Future Work

The largest limitation to the resolution of the X-ray tomography was the contrast between the propellant, reactive fiber, and voids as the X-ray system was operated at optimized values for the reactive fiber enhance propellant. However, more extensive pre-processing can be done prior to reconstruction to improve clarity of the tomographic images. Work is currently underway to utilize adaptive filtering and other methods to despeckle images while retaining sharp edges, which would result in an improved reconstruction of the surface features created by the reactive fibers by reducing noise. Furthermore, quantitative data on the changing surface area can be obtained from the reconstruction, allowing for better understanding of the evolution of the geometric effects created by the reactive fibers.

3.6 Acknowledgments

This work was funded by the National Science Foundation Graduate Research Fellowship Program grant number DGE-1333468.

3.7 References

- [1] G. F. Mangum, R. E. Rogers, and E. J. Schreck, Thiokol Corporation, Newtown, PA, U.S. Patent Application for “Method for making coated ultra-fine ammonium perchlorate particles and product produced thereby.” Docket No. 3,954,526, filed 22 Feb 1971.
- [2] Y. F. Ivanov, M. N. Osmonoliev, and V. S. Sedoi, “Productions of Ultra-Fine Powders and Their Use in High Energetic Compositions,” *Propellants, Explos. Pyrotech.*, vol. 28, no. 6, pp. 319–333, 2003, doi: 10.1002/prop.200300019.
- [3] J. R. Luman, B. Wehrman, K. K. Kuo, R. A. Yetter, N. M. Masoud, T. G. Manning, L. E. Harris, and H.A. Bruck, “Development and characterization of high performance solid propellants containing nano-sized energetic ingredients,” *Proc. Combust. Inst.*, vol. 31 II, no. 2, pp. 2089–2096, 2007, doi: 10.1016/j.proci.2006.07.024.
- [4] S. Iser, T. D. Hedman, R. P. Lucht, and S. F. Son, “Oxidizer coarse-to-fine ratio effect on microscale flame structure in a bimodal composite propellant,” *Combust. Flame*, 2016, doi: 10.1016/j.combustflame.2015.10.015.
- [5] Z. Yang, F. Gong, L. Ding, Y. Li, G. Yang, and F. Nie, “Efficient Sensitivity Reducing and Hygroscopicity Preventing of Ultra-Fine Ammonium Perchlorate for High Burning-Rate Propellants,” *Propellants, Explos. Pyrotech.*, vol. 42, no. 7, pp. 809–815, 2017, doi: 10.1002/prop.201600237.
- [6] K. Tejasvi, V. Venkateshwara Rao, Y. Pydi Setty, and K. Jayaraman, “Ultra-Fine Aluminium Characterization and its Agglomeration Features in Solid Propellant Combustion for Various Quenched Distance and Pressure,” *Propellants, Explos. Pyrotech.*, vol. 45, no. 5, pp. 714–723, 2020, doi: 10.1002/prop.201900371.
- [7] A. N. Ali, S. F. Son, M. A. Hiskey, and D. L. Naud, “Novel High Nitrogen Propellant Use in Solid Fuel Micropropulsion,” *J. Propuls. Power*, vol. 20, no. 1, pp. 120–126, 2004, doi: 10.2514/1.9238.
- [8] R. A. Yetter, G. A. Risha, and S. F. Son, “Metal particle combustion and nanotechnology,” *Proc. Combust. Inst.*, vol. 32 II, no. 2, pp. 1819–1838, 2009, doi: 10.1016/j.proci.2008.08.013.
- [9] T. R. Sippel, S. F. Son, and L. J. Groven, “Altering reactivity of aluminum with selective inclusion of polytetrafluoroethylene through mechanical activation,” *Propellants, Explos. Pyrotech.*, vol. 38, no. 2, pp. 286–295, 2013, doi: 10.1002/prop.201200102.

- [10] T. R. Sippel, S. F. Son, and L. J. Groven, Purdue Research Foundation, West Lafayette, IN, U.S. Patent Application for “Mechanically activated metal fuels for energetic material applications,” Docket No. 9,227,883, filed 31 July 2013.
- [11] M. A. Rubio, I. E. Gunduz, L. J. Groven, T. R. Sippel, C. W. Han, R. R. Unocic, V. Ortalan, and S. F. Son, “Microexplosions and ignition dynamics in engineered aluminum/polymer fuel particles,” *Combust. Flame*, 2017, doi: 10.1016/j.combustflame.2016.10.008.
- [12] B. C. Terry, I. E. Gunduz, M. A. Pfeil, T. R. Sippel, and S. F. Son, “A mechanism for shattering microexplosions and dispersive boiling phenomena in aluminum-lithium alloy based solid propellant,” *Proc. Combust. Inst.*, vol. 36, no. 2, pp. 2309–2316, 2017, doi: 10.1016/j.proci.2016.06.099.
- [13] L. T. DeLuca, “Overview of Al-based nanoenergetic ingredients for solid rocket propulsion,” *Def. Technol.*, vol. 14, no. 5, pp. 357–365, 2018, doi: 10.1016/j.dt.2018.06.005.
- [14] T. D. Hedman, D. A. Reese, K. Y. Cho, L. J. Groven, R. P. Lucht, and S. F. Son, “An experimental study of the effects of catalysts on an ammonium perchlorate based composite propellant using 5kHz PLIF,” *Combust. Flame*, vol. 159, no. 4, pp. 1748–1758, 2012, doi: 10.1016/j.combustflame.2011.11.014.
- [15] A. A. Vargeese, “A kinetic investigation on the mechanism and activity of copper oxide nanorods on the thermal decomposition of propellants,” *Combust. Flame*, vol. 165, pp. 354–360, 2016, doi: 10.1016/j.combustflame.2015.12.018.
- [16] S. Isert, C. D. Lane, I. E. Gunduz, and S. F. Son, “Tailoring burning rates using reactive wires in composite solid rocket propellants,” *Proc. Combust. Inst.*, vol. 36, no. 2, pp. 2283–2290, 2017, doi: 10.1016/j.proci.2016.06.141.
- [17] H. Wang, J. B. DeLisio, S. Holdren, T. Wu, Y. Yang, J. Hu, and M. Zachariah, “Mesoporous Silica Spheres Incorporated Aluminum/Poly (Vinylidene Fluoride) for Enhanced Burning Propellants,” *Adv. Eng. Mater.*, vol. 20, no. 2, pp. 1–7, 2018, doi: 10.1002/adem.201700547.
- [18] S. J. Barkley, D. K. Kindem, K. Zhu, J. B. Michael, and T. Sippel, “Dynamic control of composite solid propellant flame spread through microwave eddy current heating of propellant-embedded antennas,” *AIAA Scitech 2019 Forum*, no. January, pp. 1–8, 2019, doi: 10.2514/6.2019-1239.
- [19] A. E. Fogelzang, A. P. Denisyuk, V. V. Serushkin, V. Y. Egorshv, V. P. Sinditskii, and A. D. Margolin, “Burning behavior of composite propellants with fast-burning inclusions,” *J. Propuls. Power*, vol. 16, no. 2, pp. 374–376, 2000, doi: 10.2514/2.5581.
- [20] V. P. Sinditskii, V. Y. Egorshv, V. V. Serushkin, S. A. Filatov, and A. N. Chernyi, “Combustion mechanism of energetic binders with nitramines,” *Int. J. Energ. Mater. Chem. Propuls.*, vol. 11, no. 5, pp. 427–449, 2012, doi: 10.1615/IntJEnergeticMaterialsChemProp.2013005557.

- [21] V. P. Sinditskii, V. Y. Egorshchev, M. V. Berezin, V. V. Serushkin, S. A. Filatov, and A. N. Chernyi, "Combustion mechanism of nitro ester binders with nitramines," *Combust. Explos. Shock Waves*, vol. 48, no. 2, pp. 163–176, 2012, doi: 10.1134/S0010508212020062.
- [22] V. P. Sinditskii, A. N. Chernyi, D. S. Shmelev, V. Y. Egorshchev, S. A. Filatov, A. A. Matveev, and Y. M. Milekhin, "Combustion of potassium dinitramide and its binary mixtures with nitroester binder," *Combust. Flame*, vol. 172, pp. 206–214, 2016, doi: 10.1016/j.combustflame.2016.07.015.
- [23] I. E. Gunduz, M. S. McClain, P. Cattani, G. T. C. Chiu, J. F. Rhoads, and S. F. Son, "3D printing of extremely viscous materials using ultrasonic vibrations," *Addit. Manuf.*, vol. 22, no. April, pp. 98–103, 2018, doi: 10.1016/j.addma.2018.04.029.
- [24] M. S. McClain, I. E. Gunduz, and S. F. Son, "Additive manufacturing of ammonium perchlorate composite propellant with high solids loadings," *Proc. Combust. Inst.*, vol. 000, pp. 1–8, 2018, doi: 10.1016/j.proci.2018.05.052.
- [25] M. S. McClain, A. Afriat, J. F. Rhoads, I. E. Gunduz, and S. F. Son, "Development and Characterization of a Photopolymeric Binder for Additively Manufactured Composite Solid Propellant Using Vibration Assisted Printing," *Propellants, Explos. Pyrotech.*, vol. 45, no. 6, pp. 853–863, 2020, doi: 10.1002/prep.201900387.
- [26] D. N. Collard, M. S. McClain, N. A. Rahman, N. H. Dorcy, T. R. Meyer, and S. F. Son, "Dynamic X-Ray Imaging of Additively Manufactured Reactive Components in Solid Propellants," *J. Propuls. Power*, vol. d, pp. 1–7, 2020, doi: 10.2514/1.b38128.
- [27] N. Guo and M. C. Leu, "Additive manufacturing: Technology, applications and research needs," *Front. Mech. Eng.*, vol. 8, no. 3, pp. 215–243, 2013, doi: 10.1007/s11465-013-0248-8.
- [28] X. Wang, M. Jiang, Z. Zhou, J. Gou, and D. Hui, "3D printing of polymer matrix composites: A review and prospective," *Compos. Part B Eng.*, vol. 110, pp. 442–458, 2017, doi: 10.1016/j.compositesb.2016.11.034.
- [29] P. Parandoush and D. Lin, "A review on additive manufacturing of polymer-fiber composites," *Compos. Struct.*, vol. 182, pp. 36–53, 2017, doi: 10.1016/j.compstruct.2017.08.088.
- [30] K. K. B. Hon, L. Li, and I. M. Hutchings, "Direct writing technology-Advances and developments," *CIRP Ann. - Manuf. Technol.*, vol. 57, no. 2, pp. 601–620, 2008, doi: 10.1016/j.cirp.2008.09.006.
- [31] T. J. Fleck, A. K. Murray, I. E. Gunduz, S. F. Son, G. T. C. Chiu, and J. F. Rhoads, "Additive manufacturing of multifunctional reactive materials," *Addit. Manuf.*, vol. 17, pp. 176–182, 2017, doi: 10.1016/j.addma.2017.08.008.

- [32] D. N. Collard, T. J. Fleck, J. F. Rhoads, and S. F. Son, “Tailoring the reactivity of printable Al/PVDF filament,” *Combust. Flame*, vol. 223, pp. 110–117, 2021, doi: 10.1016/j.combustflame.2020.09.016.
- [33] E. Katz, A. L. Yarin, W. Salalha, and E. Zussman, “Alignment and self-assembly of elongated micronsize rods in several flow fields,” *J. Appl. Phys.*, vol. 100, no. 3, 2006, doi: 10.1063/1.2206090.
- [34] W. E. Uspal, H. Burak Eral, and P. S. Doyle, “Engineering particle trajectories in microfluidic flows using particle shape,” *Nat. Commun.*, vol. 4, pp. 1–9, 2013, doi: 10.1038/ncomms3666.

4. FLASH AND LASER IGNITION OF Al/PVDF FILMS AND ADDITIVELY MANUFACTURED IGNITERS FOR SOLID PROPELLANT

D. N. Collard, K. E. Uhlenhake, J. F. Rhoads, S. F. Son, “Flash and laser ignition of Al/PVDF films and additively manufactured igniters for solid propellant,” *12th U.S. National Combustion Meeting*, Virtual, May 24-26, 2021.

Solid propellants are employed in a range of applications, each with specific ignition requirements, from the inflation of airbags to propulsion systems for rockets. The ignition of solid propellants must be carefully controlled and modified on a per-use basis. Using tailored photoreactive materials as a source of ignition for solid propellants could reduce the added weight and risk of traditional initiators and result in safer, more effective solid rocket motor ignition systems. This study demonstrates the tunability of the ignition delay of optically-activated reactive aluminum/polyvinylidene (Al/PVDF) films and additively manufactured igniters. A single printed layer of pure nano-aluminum (nAl) at ideal stoichiometry in PVDF was found to flash ignite but frequently produced rough transitions in propagation from the igniter to the propellant. To improve the smoothness of the transition, fuel particle size, igniter thickness, and a combination of layers of nAl and micron-aluminum (μ Al) were investigated. Film formulations were investigated over a range of nAl and μ Al fuel mixtures, starting with nAl fuel at ideal stoichiometry and replacing a portion with μ Al fuel until the films would no longer flash ignite. Igniters were printed with fused filament fabrication (FFF) in configurations of up to 5, 0.125 mm layers of Al/PVDF, specifying the fuel as either purely nAl, μ Al, or a mixture of both. In printed igniters with layers of μ Al, only a single layer of nAl was needed to flash ignite the material and propagate to the layers of μ Al without delay. These films and printed igniters were then cast onto strands of ammonia perchlorate composite propellant and the ignition delays were quantified. The steadiest propagation was achieved with a single layer of nAl printed atop a triple layer of μ Al for the flash-activated propellant and a single layer of nAl printed atop a single and triple layer of μ Al for laser-driven igniters.

4.1 Introduction

The ignition of energetic materials is a complex process that must be adaptable to a variety of use cases. Pyrotechnics, propulsion, and munitions all have unique requirements for safe and controlled ignition. As a result, many distinct ignition strategies are employed, including percussion devices, bridgewire igniters, and sensitive pyrotechnic initiators (pyrogens) [1]. Optical ignition is of interest as it can reduce the input energy needed for ignition while providing more spatial and temporal control and improve safety by eliminating the electrical systems used in pyrogens and bridgewires, thereby reducing the risk associated with stray electrical charges.

Optical ignition can be classified into two categories: broadband, scattered light energy dubbed flash ignition, and coherent, single wavelength energy referred to as laser ignition. Nanoscale metal particles, carbon nanotubes, high-nitrogen materials, and thin films of nanoporous silicon have been shown to ignite with a broadband light source [2-6]. However, flash ignition has only been successful with loose powders or low-density materials, which are difficult to integrate into practical energetic systems. Previous work [7] has shown that nAl/PVDF is a full-density composite that retains its flash ignition capabilities due to the PVDF binder isolating the nAl particles.

Laser ignition is easier to implement into practical energetic systems due to the higher energy output capabilities compared to broadband light sources; however, the sensitivity of energetic materials to energy flux from the laser can lead to a variety of problems during ignition. For example, double-base nitrocellulose propellants require a critical and narrow window of flux intensity, an “ignition corridor”, for self-sustained ignition [8]. Below the critical energy, the propellant will not ignite. Above, the reaction is overdriven, resulting in extinguishment when the laser flux is removed. Similar regimes of ignition were found in aluminized AP composite propellant [9]. Additionally, ignition delay varies greatly with input energy, pressure, and material formulation [8-10].

Both ignition delay control and self-sustained ignition are crucial for practical propellant systems. A possible solution for consistent laser ignition is the use of an absorptive coating. Carbon black has been used to increase the absorptivity of propellants at the surface [11]. When used as a coating or additive, carbon black has improved ignition in a range of wavelengths from 500-1064 nm [12-13]. Additionally, carbon black has been used to reduce ignition thresholds and delays in secondary explosives [14]; however, its use is limited in energetic materials due to its small particle

size, which can lead to increased porosity and agglomeration. Furthermore, carbon black is a relatively inert material, resulting in decreased energetic performance.

In this study, the optical ignition of solid propellants was explored by introducing a cap of photo-sensitive reactive material to the top of propellant strands. The reactive material was composed of nAl/PVDF, which was tape cast and 3-D printed to ensure precise control over the geometry and thickness. The consistency of self-sustained ignition and ignition delay were studied in flash and laser-driven systems. Additionally, formulations with a mixture of nAl and μ Al fuel and 3-D printed layers of either nAl or μ Al fuel were investigated for improved ignition properties.

4.2 Experimental Methods

Thin films of 20 wt.% Al/PVDF were prepared with nAl and μ Al fuel. Nine formulations of films were made by varying the active nAl (80 nm nominal diameter, 70% active content, Novacentrix) content in the fuel by 12.5 wt.% with the remaining fuel consisting of μ Al (3 μ m, Valimet H-3). Powdered PVDF (Kynar 711, Arkema) was dissolved in dimethylformamide (DMF) at a solvent ratio of 6:1 mL per gram PVDF. Aluminum was added to DMF then ultrasonically mixed (Branson Digital Sonifier) for 3 min before adding PVDF and followed with a second mixing cycle. The solution was cast into thin films using a tape caster (MIT Corporation MSK-AFA-HC100) with a heated bed held at 125 °C to ensure full-density films. The films were dried on the heated bed for 15 min before removing and drying overnight at ambient conditions.

Seven structures of igniters were tested for ignition delays on propellants: two tape-cast and five printed formulations. All of the igniter formulations had an active content of 20 wt.% aluminum in PVDF. The tape-cast films consisted of purely nAl and a mixture of nAl and μ Al fuel in which 75 wt.% of the fuel content was nAl and 25 wt.% μ Al (0.75 nAl film), resulting in thicknesses between 20-30 μ m. Printed igniter formulations included single-layer nAl (1 nAl), five-layer nAl (5 nAl), single-layer nAl on top of a single-layer of μ Al (1 nAl x 1 μ Al), single-layer nAl on top of three layers of μ Al (1 nAl x 3 μ Al) and single-layer nAl and μ Al mixture (0.75 nAl).

Printable filament material was prepared as detailed in previous work [15-16]. The filament was printed into 1 cm x 1 cm igniters through fused-filament fabrication (FFF) with a print speed of 10 mm/s and layer height of 0.125 μ m. The filament was passed through an extruder head heated

to 240 °C and deposited onto a heated build plate maintained at 70 °C with a BuildTak 3-D Printing Surface supplemented by a layer of glue (Elmer's All Purpose Glue).

The igniters were cast on composite propellant comprising of 85 wt.% ammonia perchlorate (AP) with a 4:1 coarse (60-130 μm , Firefox) to fine (20 μm , ATK) ratio and 15 wt.% binder. The binder consisted of 76.33 wt.% hydroxyl-terminated polybutadiene (R45-M HTPB, Rocket Motor Components), 15.05% isodecyl pelargonate plasticizer (Rocket Motor Components), and 8.62% isophorone diisocyanate curing agent (Firefox). Batches of 35 g were prepared with an initial hand mixing followed by a two, 3 min cycles on a resonant mixer (LABRAM Resodyn) at 80 g under vacuum. Propellant was cast into a polytetrafluoroethylene mold with dimensions of 2.54 cm x 7.62 cm x 0.64 cm with one side exposed. Igniters were laid on top of the propellant with the top nAl layer exposed then covered. The mold was compressed until propellant no longer pushed through the overflow holes. No intermediate adhesive was used to hold the igniters in place. A minimum of ten propellant samples were fabricated for each igniter formulation.

Flash testing of the nAl and μAl mixture films was conducted using a broadband xenon flash lamp (White Lightning X3200, Paul C. Buff Inc.). Films were cut into 1 cm x 1 cm squares and placed in front of the flash bulb at a set distance. Due to the scattering of the broadband light, the deposited energy was controlled by distance, up to a maximum of 2 cm. The flash lamp was then triggered and ignition of the films was selectively observed. The placement of each sample was determined using Neyer's Sensitivity Test [17]. A minimum of 30 samples were tested to determine the minimum ignition energy (MIE) resulting in a 50% probability of ignition with a two-sided confidence interval of 95%. These tests were then repeated for 1 nAl printed igniters of the same dimensions.

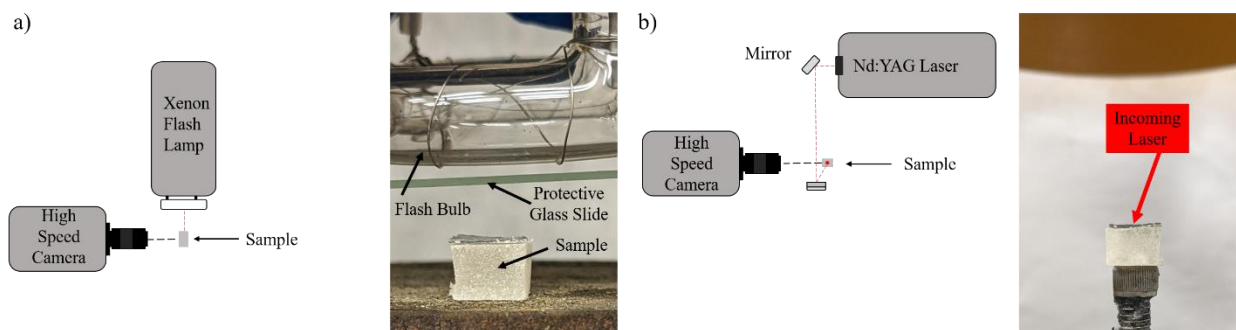


Figure 4.1. The experimental setup associated with the experiments for (a) flash ignition and (b) laser ignition.

A similar test setup was utilized for flash ignition of solid propellants (Figure 4.1a). The propellants were placed below the flash lamp with the igniter facing the xenon flash bulb. A thin glass slide was placed between the propellant and the flash bulb to protect the bulb from the high temperatures of the propellant flame. The flash lamp was then triggered and observed at 2500 fps with a high-speed camera (Phantom v2012). The incident flash energy was roughly 7 J/cm^2 . Ignition delay was defined as the first light on the Al/PVDF igniter to an evenly propagating flame across the entire the AP composite propellant surface.

These tests were then repeated with a laser system (Figure 4.1b) to observe ignition from a highly focused heating source and remove the need for a protective glass slide. The samples were ignited with a Nd:YAG laser [18] operating at a wavelength of 1064 nm and energy of 7 J/cm^2 fired in a pulse burst mode with a 5 ms burst, 10 ns pulses, and a repetition rate of 100 kHz. These settings roughly match the temporal profile of the flash bulb. Ignition delay was defined the same as with flash ignition.

Surface roughness measurements were taken on films and 3D printed materials using a profilometer (Alpha-Step D-600). The profilometer was able to detect changes in surface height on the scale of nanometers and produce profile traces of the materials. These profile traces were used to capture general roughness and surface features to compare the films to the printed materials. A numeric integration of these profiles was done to obtain a total surface length that would be exposed to the optical energy input.

4.3 Results and Discussion

An igniter needs to consistently initiate the propagation of the main body of the energetic material. Dimming, quenching, and unsteady transitions are undesirable as they lead to increased variability in performance. The second primary factor is the delay between initiation and ignition of the main energetic material. To characterize the Al/PVDF film and printed igniters, the minimum ignition energy (MIE), ignition delay, and consistency of transition from igniter to an AP composite propellant were quantified.

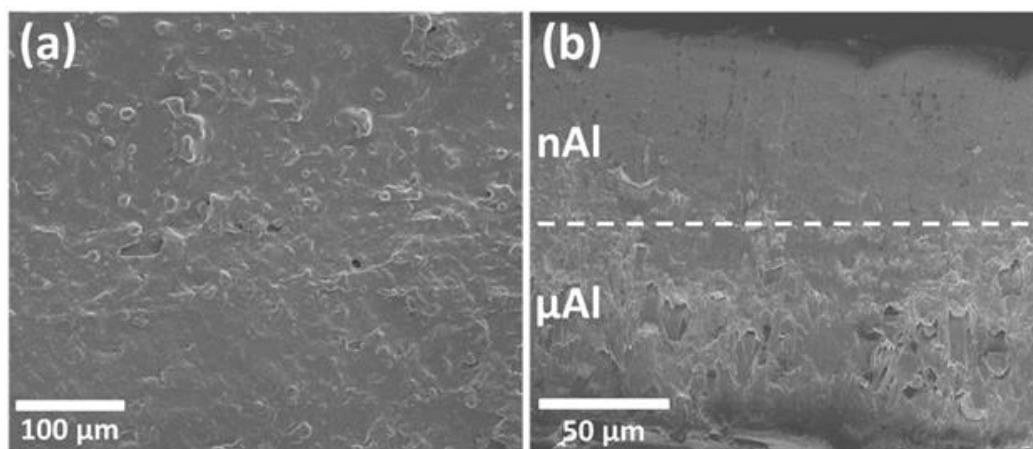


Figure 4.2. Microscopic images of (a) the top of a printed nAl layer (b) a dual layer igniter with one layer of nAl on top of one layer of μ Al.

Printed igniters with layers of nAl and μ Al were examined with scanning electron microscopy (SEM) to investigate the samples' surface and internal structure. The surface of the printed nAl igniter (Figure 4.2a) had a higher roughness than the tape-cast films of the same formulation. To examine a dual-layer cross-section, the igniters were cut with a razor blade. The nAl and μ Al were identifiable by the microstructure as seen in Figure 4.2b. In the layer of μ Al, Al particles can be seen displaced from their original positions due to the blade cut, and the tracks left during the displacement were not indicative of porosity before the cut.

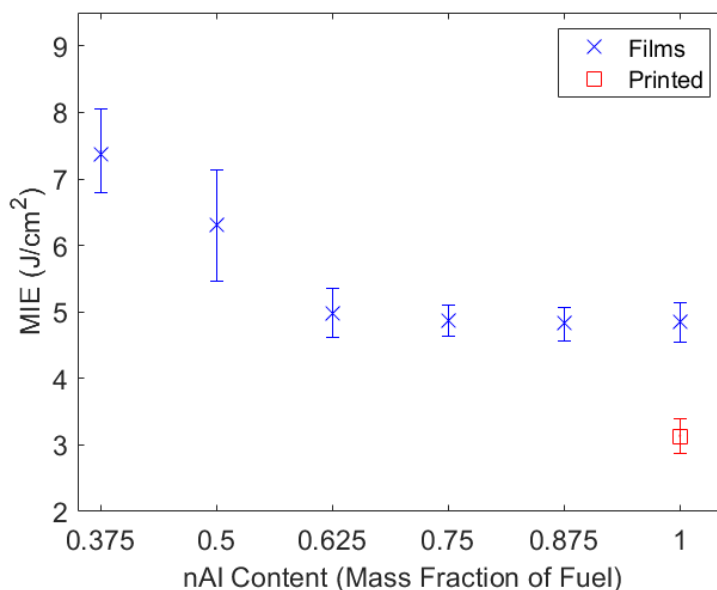


Figure 4.3. The minimum ignition energy of films at varying concentrations of nAl and μ Al fuel.

The effect of Al size on flash ignition can be seen in Figure 4.3. There are two key thresholds for flash ignition: the minimum mass fraction of nAl needed to flash ignite and the asymptotic decline of MIE as nAl increased. The interaction of light energy in the film is scattering dominated with μAl and absorption dominated with nAl [6-7]. Below a mass fraction of 0.375 nAl, no films ignited as most of the energy is scattered and too little is absorbed by the nAl to ignite it. At a mass fraction 0.625 nAl, the MIE drops to $\sim 5 \text{ J/cm}^2$ and remains constant as the nAl mass fraction increases. While ignition was observed at a nAl mass fraction of 0.375 and 0.50, these samples had higher MIE and variability. However, once the nAl mass fraction reached 0.625, the highly absorptive nAl particles dominated the interaction with the light energy. While there is still some μAl , the light scattering does not hinder the absorption and the MIE remains constant. Additionally, the MIE for a 1 nAl printed igniter is significantly lower than films of the same composition.

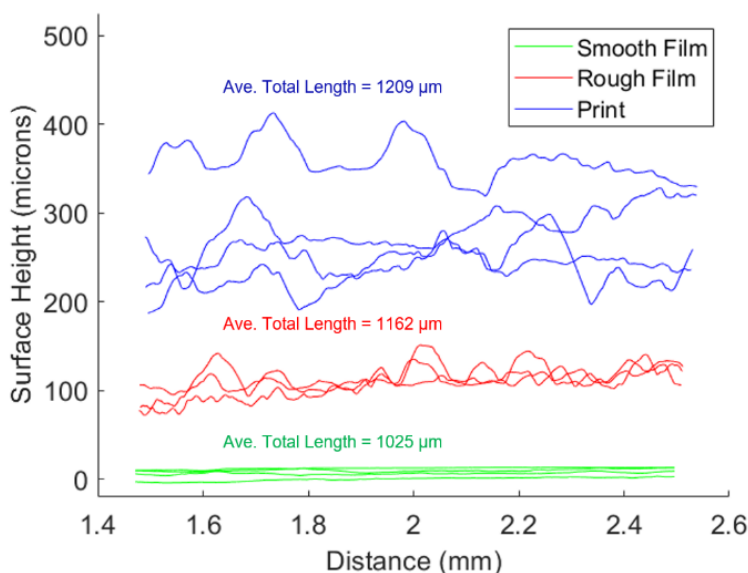


Figure 4.4. Profilometer measurements obtained from nAl films and printed 1 nAl. The average total length is a numerical integration of the surface profile and is used to get an estimate of the total length exposed to the flash. Integrations were done over a 1 mm length portion of the data and averaged.

The surface roughness of the samples may affect the sensitivity. The process of tape-casting nAl samples produces two surface finishes: the side of the film exposed to air produces a rough surface, while the side of the film touching the glass plate produces a smooth surface. The

printed samples have a more visibly rough surface as a result of the print lines and nozzle limitations. As can be seen in Figure 4.4, the printed samples exhibited low-frequency, high-amplitude surface variations, while the rough side of the films exhibited higher-frequency and low-amplitude variations. The rough side of the films and the printed samples had similar total surface length despite different MIE, indicating that the surface length was not solely responsible for the difference, but rather the manner of the surface roughness. With high amplitude variation, light reflected from the sample has a higher chance to collide with another surface, globally increasing the amount of energy absorbed by the surface and lowering the MIE. The smooth and rough side of the films showed no significant differences in MIE despite the increase in total surface length, reinforcing that the low-amplitude variation on the rough side may not have been large enough to capture a significant amount of reflected light.

The Al/PVDF igniters commonly exhibited three modes of transition when igniting the AP composite propellant: 1) an unsuccessful ignition of the propellant pellet, 2) a rough transition which resulted in the rapid consumption of the igniter material followed by a diminished reaction on the propellant before recovering across the pellet, and 3) a smooth transition from the reaction of the igniter material to steady reaction of the propellant pellet. All of the pellets with film igniters failed to ignite the propellant as the film was consumed too quickly for sufficient energy to transfer into the propellant for continued reaction. The tape-cast fabrication method limited the films to a thickness of 20-30 μm which proved to be insufficient for the reaction to transfer into the propellant.

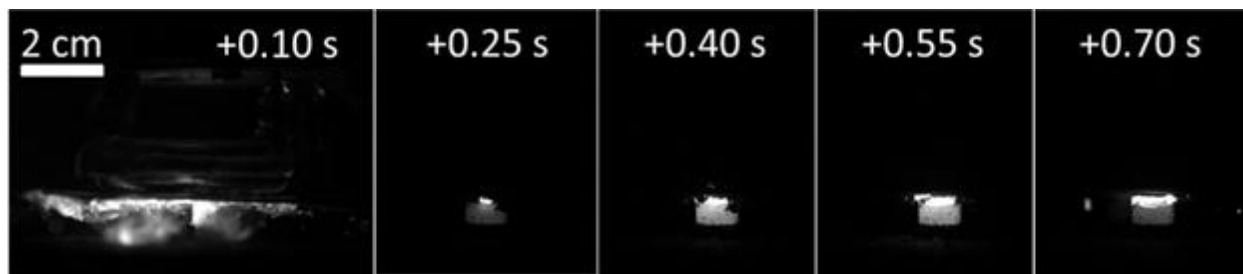


Figure 4.5. The progression of a printed 1 nAl igniter exhibiting a rough transition between ignition of the nAl/PVDF and propellant.

The ignition delay of the igniter-propellant system was defined as the time from first light on the igniter to the observation of steady flame propagation across the entire propellant pellet surface. The aluminized material was brighter and had a different flame structure than that of the

AP composite flames, allowing for the identification of the transition between the igniter and propellant. Frames were manually identified leading to an associated error for each test based on the range of frames involving the first signs of AP propellant flames across the entire surface to the consumption of any lingering Al/PVDF. In Figure 4.5, a recovered flame on the propellant pellet can be seen in the third frame around 0.4 s.

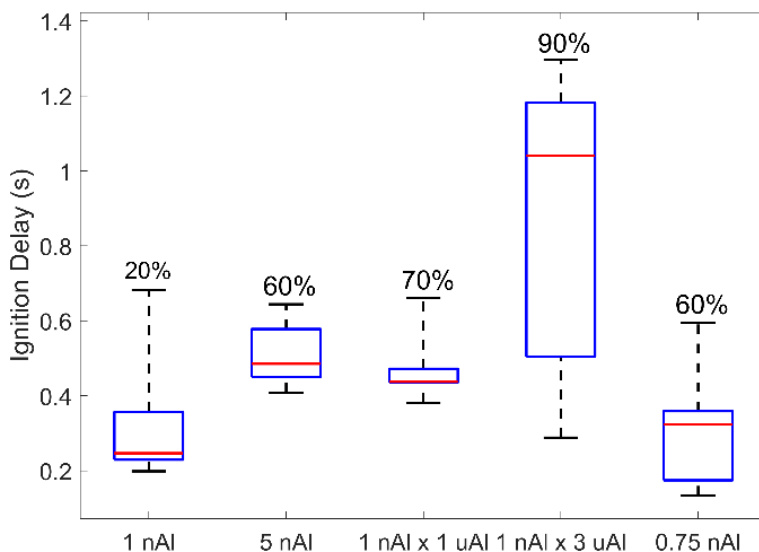


Figure 4.6. The flash ignition delays of printed igniters with the percentage of smooth transitions indicated.

The printed igniters consisting of 1 nAl and 5 nAl exhibited a rough transition (Figure 4.6) between the igniter and propellant reactions for 20% and 60% of the samples, respectively. As shown in Figure 4.6, the increased thickness of the 5 nAl resulted in a higher average ignition delay than the 1 nAl (0.51 s and 0.31 s); however, despite the increased time for the reaction to proceed through the layers of the igniter material, the 5 nAl igniters led to more samples exhibiting a smooth transition between the igniter and propellant, but not all. A single layer of 0.75 nAl was also found to exhibit a similar percentage of samples with smooth reaction transition between the igniter and the propellant as 5 nAl, but with a reduced average ignition delay time. This indicated that the speed of reaction may not be solely responsible for determining the quality of the transition between materials.

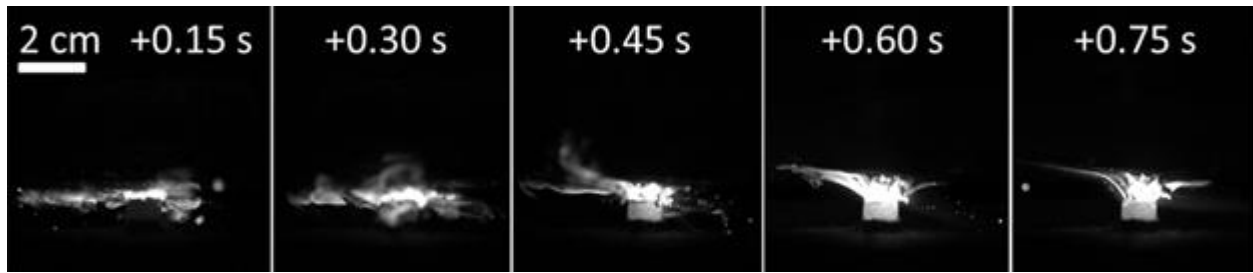


Figure 4.7. The progression of a printed 1 nAl x 1 μ Al igniter exhibiting a smooth transition between the first light on the igniter and the steady burning of the propellant.

To address the need for a smooth transition from the flash ignition of the nAl layer to flame propagation in the propellant, a layer of μ Al was added below the nAl. Formulations of μ Al have been shown to react slower than nAl [16]; however, μ Al has been shown to not flash ignite [4]. In Figure 4.7, a layer of nAl was needed to begin the reaction and a single layer was shown to smoothly transition into the μ Al layer below followed by another smooth transition into the reaction of the propellant pellet. The layered igniter 1 nAl x 1 μ Al performed similarly to the 5 nAl igniter (Figure 4.6) with a similar number of samples with diminished reaction in the transition between igniter material and propellant. Increasing the μ Al layers to three resulted in a longer ignition delay than the 1 nAl x 1 μ Al as more material had to be consumed before reaching the propellant pellet. The 1 nAl x 3 μ Al samples had more consistently smooth transitions but had the largest average and spread of ignition delays of the formulations tested. Only one sample of 1 nAl x 3 μ Al exhibited a diminished transition into the propellant sample.

Table 4.1. Flash ignition delays and propagation modes.

Igniter Setup	Total Ignition Delay (s)		Associated Error per Test (s)	% Smooth Transition
	Average	Std Dev		
1 nAl	0.33	0.18	0.01	20%
5 nAl	0.51	0.08	0.02	60%
1 nAl x 1 μ Al	0.47	0.09	0.03	70%
1 nAl x 3 μ Al	1.04	0.30	0.03	90%
1 nAl/ μ Al Mix	0.36	0.13	0.03	60%
nAl/ μ Al Mix Film	No Propellant Ignition			0%
nAl Film	No Propellant Ignition			0%

The associated error per test (Table 4.1) increased with the addition of μ Al layers due to the occasional lingering of burning tendrils of Al/PVDF on the surface of the propellant. As nAl

reacts rapidly, the soot formed locally around the aluminum is blown apart into smaller solid fragments, whereas micron aluminum typically exhibits soot formation in long, connected strands [16]. As a protective glass slide had to be placed close to the igniters, there was concern that the glass may be inhibiting the propellant by obstructing the release of soot from the reaction zone. To investigate if the protective slides were inhibiting the reactions and creating the dimming transitions, ignition delay tests were repeated with a laser setup.

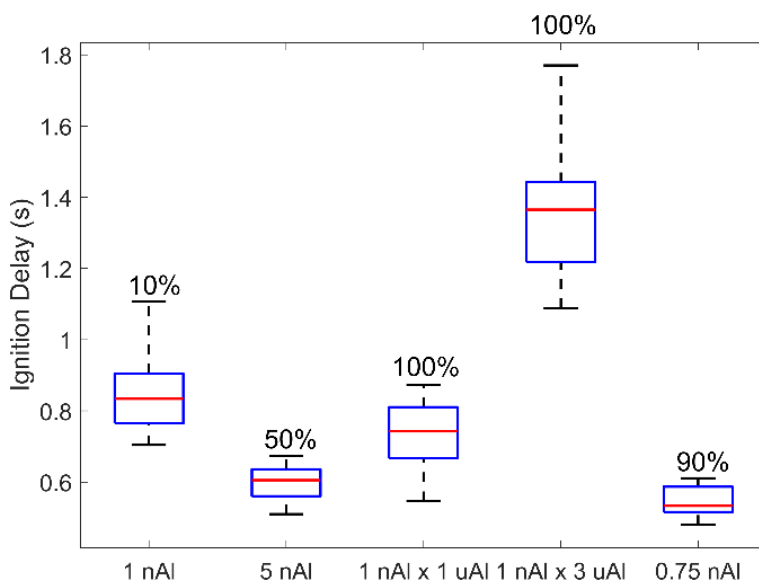


Figure 4.8. Laser ignition delays of printed igniters with the percentage of samples with smooth transitions indicated.

The laser drives ignition at energies higher than the MIE of the Al/PVDF igniter materials and the optical setup removes the necessity of a protective glass slide altogether. If the rough transitions in the flash ignited propellants was due to an inhibition of reaction by the glass slide, the laser materials should have significantly fewer samples with rough transitions than its flash counterparts. Although 1 nAl x 1 μ Al, 1 nAl x 3 μ Al and 0.75 nAl printed igniters exhibit smoother transitions in Figure 4.8 compared to the flash ignited samples in Figure 4.6, the 1 nAl and 5 nAl do not, indicating that the slide was not responsible for the dimming transitions. Rather this may be an artifact of the limited sample size or due to the higher energies used to initiate the reaction.

Table 4.2. Laser ignition delays and propagation modes.

Igniter Setup	Total Ignition Delay (s)		Associated Error per Test (s)	% Smooth Transition
	Average	Std Dev		
1 nAl	0.84	0.12	0.02	10%
5 nAl	0.61	0.05	0.02	50%
1 nAl x 1 μ Al	0.72	0.10	0.02	100%
1 nAl x 3 μ Al	1.32	0.13	0.03	100%
1 nAl/ μ Al Mix	0.54	0.05	0.02	90%
nAl/ μ Al Mix Film	No Propellant Ignition			0%
nAl Film	No Propellant Ignition			0%

With the limited sample size, the 1 nAl x 1 μ Al samples had the lowest ignition delay of 0.72 s (Table 4.2) for the most consistent transitions between igniter and propellant of laser-ignited samples. In major part due to the number of rough transitions pulling the average higher, the laser-ignited 5 nAl samples had shorter delay times than the 1 nAl despite the fewer number of layers. Rough transitions tended to increase the time until the flame recovered across the propellant, but were not always reflected in the standard deviation of ignition delay between samples.

A single layer igniter with a mixture of nano- and micro-scale fuel (0.75 nAl) was also found to exhibit a smooth reaction transition between the igniter and the propellant in the majority of laser-ignited samples. This Al/PVDF formulation has been shown previously [16] to propagate at a rate similar to formulations with only nAl. This indicates that size of the Al fuel has a critical role in transferring energy from the reaction of the igniter to the propellant to produce a smooth transition and the transition does not depend solely on slowing down the propagation of the reaction.

4.4 Conclusions

Tests of minimum ignition energy show a minimum nAl content necessary for initiation of Al/PVDF films of 20 wt.% fuel content. As nAl content is increased, the minimum ignition energy approaches an asymptote. Printed igniters achieve ignition at lower energies due to their increased surface roughness of high amplitude, low frequency surface deviations that worked as a light trap, absorbing more otherwise reflected light.

Films of 20-30 μm thick nAl were unable to ignite AP composite propellant pellets due to their rapid consumption and poor transfer into the underlying propellant. Printed igniters of ~ 125 μm and greater thicknesses ignited propellant pellets; however, many exhibited poor energy transfer to the propellant pellets, resulting in an unsteady, dimming flame as the reaction front transitioned from the igniter to the propellant before finally recovering across the entire propellant.

Despite its fast consumption, thin layers of nAl material propagate readily to layers of μAl , but did not consistently propagate smoothly into AP composite propellant. To get smooth, consistent transitions from igniter to propellant reaction, a multi-layered igniter was necessary. To flash ignite, the first layer exposed to the flash bulb needed a critical mass fraction of nAl of 0.375 to initiate reaction. Subsequent layers consisting of μAl slow down the propagation rate, increasing the time for heat to transfer to the composite propellant and result in consistently smoother propagation from igniter to propellant. When initiating with a laser driven at higher energies, a consistent and smooth transition was achieved with fewer μAl layers.

4.5 Acknowledgments

This work was funded by the National Science Foundation Graduate Research Fellowship Program grant number DGE-1333468 and AFOSR MURI award number FA9550-19-1-0008. This paper is dedicated to the memory of Dr. Brad Forch who pioneered laser ignition of propellants.

4.6 References

- [1] D.H. Barrett, Solid rocket motor igniters, Report No. NASA SP-8051, National Aeronautics and Space Administration, Lewis Research Center, Cleveland, OH, USA, 1971.
- [2] P.M. Ajayan, M. Terrones, A. De la Guardia, V. Huc, N. Grobert, B.Q. Wei, H. Lezec, G. Ramanath, T.W. Ebbesen, Nanotubes in a flash-ignition and reconstruction, *Science* 296 (2002) 705.
- [3] M.R. Manaa, A.R. Mitchell, P.G. Garza, P.F. Pagoria, B.E. Watkins, Flash ignition and initiation of explosives-nanotubes mixture, *J. Am. Chem. Soc.* 127 (2005) 13786–13787.
- [4] Y. Ohkura, P.M. Rao, X. Zheng, Flash ignition of Al nanoparticles: mechanism and applications, *Combust. Flame.* 158 (2011) 2544–2548.
- [5] Y.X. Liu, D. Liu, G.N. Liu, Energy conversion and ignition of iron nanoparticles by flash, *Sci. China Technol. Sci.* 60 (2017) 1878–1884.

- [6] Y. Ohkura, J.M. Weisse, L. Cai, X. Zheng, Flash ignition of freestanding porous silicon films: effects of film thickness and porosity, *Nano Lett.* 13 (2013) 5528–5533.
- [7] K. Uhlenhake, D. Olsen, M. Gomez-Gomez, M. Ornek, M. Zhou, S. Son, Optical ignition of nano-aluminum PVDF films using photoflash and laser energy, 12th U.S. National Combustion Meeting (2021), paper 128NCT-0019.
- [8] L. DeLuca, T. J. Ohlemiller, L. H. Caveny, M. Summerfield, Radiative ignition of double base propellants: II. Pre-ignition events and source effects, *AIAA J.* 14 (1976) 1111–1117, doi: 10.2514/3.7193.
- [9] M. Harayama, T. Saito, A. Iwama, Ignition of composite solid propellant at subatmospheric pressures, *Combust. Flame*, 52 (1983) 81-89, doi: 10.1016/0010-2180(83)90122-0.
- [10] L. DeLuca, L.H. Caveny, T.J. Ohlemiller, M. Summerfield, Radiative ignition of double-base propellants: I. Some formulation effects, *AIAA J.* 14 (1976) 940–946, doi: 10.2514/3.7167.
- [11] A.D. Baer, N.W. Ryan, Ignition of composite propellants by low radiant fluxes, *AIAA J.* 3 (1965) 884–889, doi: 10.2514/3.3011.
- [12] S. Rafi Ahmad, D. A. Russell, C. J. Leach, Studies into laser ignition of unconfined propellants, *Propellants, Explos. Pyrotech.*, 26 (2001) 235–245.
- [13] A. Kakami, R. Hiyamizu, K. Shuzenji, T. Tachibana, Laser-assisted combustion of solid propellant at low pressures, *J. Propuls. Power*, 24 (2008) 1355–1360, doi: 10.2514/1.36458.
- [14] X. Fang, W. G. McLuckie, Laser ignitibility of insensitive secondary explosive 1,1-diamino-2,2-dinitroethene (FOX-7), *J. Hazard. Mater.*, 285 (2015) 375–382, doi: 10.1016/j.jhazmat.2014.12.006.
- [15] T.J. Fleck, A.K. Murray, I.E. Gunduz, S.F. Son, G.T.C. Chiu, J.F. Rhoads, Additive manufacturing of multifunctional reactive materials, *Addit. Manuf.*, 17 (2017) 176–182, 2017, doi: 10.1016/j.addma.2017.08.008.
- [16] D.N. Collard, T.J. Fleck, J.F. Rhoads, S.F. Son, Tailoring the reactivity of printable Al/PVDF filament, *Combust. Flame*, 223 (2021) 110–117, doi: 10.1016/j.combustflame.2020.09.016.
- [17] B.T. Neyer, More efficient sensitivity testing, Miamisburg, OH, USA, 1989.
- [18] M.E. Smyser, K.A. Rahman, M.N. Slipchenko, S. Roy, T.R. Meyer, Compact burst-mode Nd:YAG laser for kHz–MHz bandwidth velocity and species measurements, *Opt. Lett.* 43 (2018) 735.

5. SUMMARY

There are many avenues to tailor solid propellant to meet a variety of end-use cases. This work investigated the successful use of reactive components to increase the burning surface area of the propellant to the burning front and to photo-ignite propellant strands. With the application of internal reactive elements in propellant also comes myriad challenges ranging from diagnostic limitations to material suitability for given manufacturing techniques and applications.

To address the diagnostic limitations of traditionally used visible imaging techniques, a dynamic X-ray imaging system was developed for the analysis of in-situ multi-component solid propellant systems that would be more representative of actual propellant systems. While the reactive components explored in this work laid the groundwork for quantification of geometric effects created by widely disparate burning rates, the material composition may not be the most suitable for rocket applications. Formulation of better performing, less sooty fast-burning materials may be needed before implementation in rockets, but the reactive-propellant systems in this work examines the fundamental methods by which the effective burning rate may be increased and analyzed.

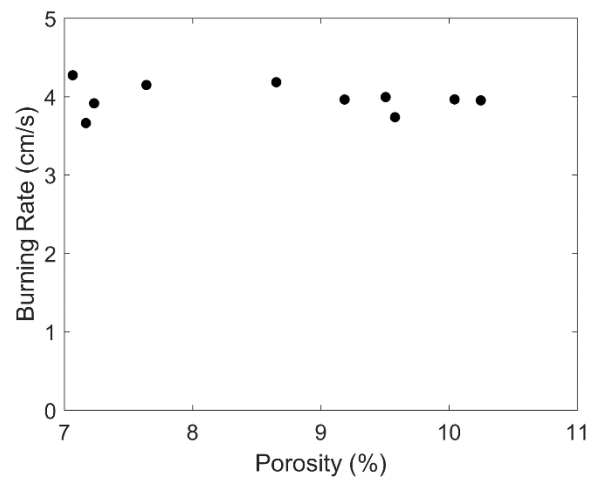
Furthermore, novel materials and methods are often adopted in industry in a stepwise manner, introducing one new “variable” at a time. Although AP composite propellant used throughout this work has been well characterized, the Al/fluoropolymer reactive material has been a relatively recent development. Many studies have examined the material and still more development is needed before adoption in end-use cases, so if a more suitable material for propellants is identified in the laboratory, it will first have to face similar rigorous examination. Yet this is a positive step forward towards another avenue of geometric tailorability.

APPENDIX A. SUPPLEMENTAL MATERIAL: TAILORING THE REACTIVITY OF PRINTABLE Al/PVDF FILAMENT

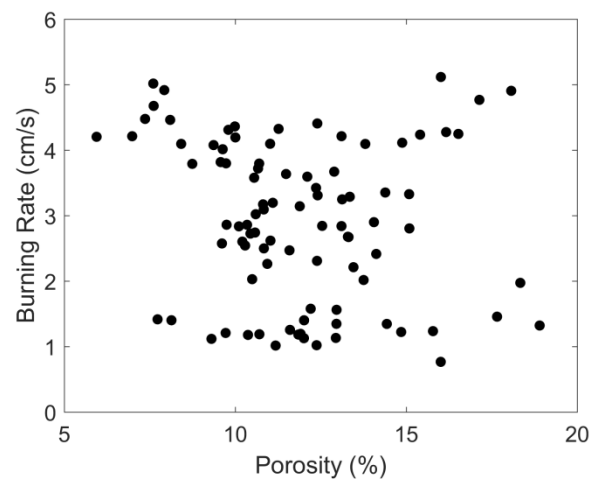
Further tests were conducted on 20 wt% nAl and 0.625 nAl to assess batch consistency and to confirm that porosity fluctuations were not the primary contributor to the variation in burning rates. It must be noted that 50 nm aluminum particles are no longer commercially available. Due to this, 80 nm aluminum was used for these supplementary tests. All of the other materials and methods were kept as described in the body of the work. Unfortunately, this means that direct and absolute comparisons cannot be made, and thus this material is included only as supplemental material.

One batch of 20 wt% nAl and ten batches of 0.625 nAl were tested to assess porosity and burning rates. In each batch, ten filament sample cross-sections were examined under a microscope followed by a digital measurement of the porosity to investigate porosity fluctuations both within the batch and between batches. The ten filament samples were then tested for combustion performance. In both formulations, as shown in Supplemental Figure A.1 and Supplemental Figure A.2, no significant correlation between burning rate and porosity was seen. Within the batch of 20 wt% nAl filament, no significant change in burning rate occurred across a porosity range of 3.2% as seen in Supplemental Figure A.1. The ten samples of filament led to an intra-batch porosity average of 8.6% with a standard deviation of 1.2% and an intra-batch burning rate of 3.98 cm/s with a standard deviation of 0.18 cm/s.

Furthermore, in Supplemental Figure A.2, across the one hundred individual filament tests of 0.625 nAl, the variation in burning rate and porosity shows no correlation. The average burning rate and standard deviation of burning rates across all of the filaments and batches of 0.625 nAl were 2.80 cm/s and 1.25 cm/s, respectively. The average porosity of all 0.625 nAl filaments was 11.9% with a standard deviation of 2.1%.



Supplemental Figure A.1. Filament porosity and burning rate of individual strands of 20 wt.% nAl/PVDF.



Supplemental Figure A.2. Filament porosity and burning rate of individual strands of 0.625 nAl.

APPENDIX B. SUPPLEMENTAL MATERIAL: DYNAMIC X-RAY IMAGING OF ADDITIVELY MANUFACTURED REACTIVE COMPONENTS IN SOLID PROPELLANT

Although there are concerns that burning samples with multiple reactive wires at higher pressures could cause sliver detachment, we do not anticipate that sliver formation and ejection would be fundamentally different from atmospheric pressure to high-pressure burning. This may be counter-intuitive, but a simple analysis shows the formation of detached slivers would rely on the type of reactive wires, relative burning rates, and the spacing. At high pressures, gas velocity decreases as density increases linearly with pressure, assuming an ideal gas. If considering drag force as the major proponent to the dislodging of slivers, a quick calculation can be considered, assuming drag can be approximated as flow over a plate. Starting with drag force on a flat plate at turbulent conditions (higher than for laminar conditions), the force is proportional to 9/5-power of the approach velocity and 5/4-power of gas density as follows [1],

$$F_{drag, flat\ plate, turbulent} \propto \sqrt[5]{\rho_g^4 \mu L^4 W^5 u^9} \quad (1)$$

$$F_{drag} \propto \rho_g^{4/5} u^{9/5} \quad (2)$$

Considering mass conservation,

$$\dot{m}_{in} = \dot{m}_{out} \quad (3)$$

Or

$$\rho_c r_b = \rho_g u \quad (4)$$

Rearranging and using the following relationships $r_b = aP^n$, $\rho_g = f(P) = \frac{PMW_{mix}}{R_u T}$, and assuming $\rho_c \neq f(P)$, we find,

$$u = \frac{a \rho_c R_u T}{MW_{mix}} P^{n-1} \quad (5)$$

And therefore,

$$F_{drag} \propto C P^{\frac{4}{5}} P^{\frac{9}{5}(n-1)} \propto P^{\frac{9}{5}n-1} \quad (6)$$

Assuming a relatively typical pressure exponent of $n = 0.35$ for a solid propellant, the drag force due to pressure effects on the density and gas velocity decreases. There is still a dependence of the drag force on the length and width of the slivers, which can be tuned with the choice of reactive material and the spacing, but this affect can still be examined by choice of propellant and reactive wire at 1 atm. Therefore, results that show a lack of detached slivers at 1 atm would also imply a lack of detached slivers at elevated pressure.

Supplemental References

- [1] Bird, B. R., Stewart, W. E., and Lightfoot, E. N., *Transport Phenomena*, 2nd ed., John Wiley & Sons, Inc., Hoboken, NJ, 2006.